



UNIVERSITÀ POLITECNICA DELLE MARCHE

FACOLTA' DI INGEGNERIA
Corso di Laurea in Ingegneria Informatica e dell'Automazione

**SINCRONIZZAZIONE DI SISTEMI
NON LINEARI DEL SECONDO ORDINE
SU MANIFOLD RIEMANNIANI
ATTRAVERSO UN CONTROLLO PID
NON LINEARE**

**SYNCHRONIZATION OF
SECOND-ORDER NON LINEAR SYSTEMS
ON RIEMANNIAN MANIFOLDS
BY NON-LINEAR PID CONTROL**

**Relatore:
Chiar.mo Prof.
SIMONE FIORI**

**Correlatore:
Dr. HWEE KUAN LEE**

**Presentata da:
MATTIA IPPOLITI
S1077863**

Anno Accademico 2018/19

*The most beautiful thing we can experience
is the mysterious. It is the source of
all true art and science
— A. Einstein, Physicist*

Contents

1	Introduction	1
2	Dynamical systems on manifolds and Lie groups	4
2.1	Notation in manifold calculus	4
2.2	Second-order dynamical systems on manifolds and Lie groups . .	5
3	Numerical simulation of second-order non-linear systems	8
3.1	Classical forward Euler, Heun and Runge methods	8
3.2	Numerical simulation of second-order non-linear systems on manifolds by forward Euler, Heun and Runge techniques	10
4	Potential energy functions and associated abstract oscillators on manifolds	13
4.1	Simple pendulum	13
4.2	Van der Pol oscillator	14
4.3	Duffing-type oscillators	15
4.4	Keplerian oscillator	17
5	Numerical simulation on the unit hypersphere	19
5.1	Numerical simulation on the simple pendulum	20
5.2	Numerical simulation on the hard Duffing oscillator	22
5.3	Numerical simulation on the soft Duffing oscillator	24
5.3.1	Euler method	24
5.3.2	Heun method	26
5.3.3	Runge (RK2) method	26
5.4	Numerical simulation on the double-well Duffing oscillator	28
5.5	Numerical simulation on the Van der Pol oscillator	30
5.6	Numerical simulation on the Kepler oscillator	32

6	Numerical simulation on the special orthogonal group $SO(3)$	35
6.1	Visual rendering via a group action on a manifold	36
6.2	Numerical simulation on the simple pendulum	36
6.3	Numerical simulation on a hard Duffing oscillator	38
6.4	Numerical simulation on the Van der Pol oscillator	40
6.5	Numerical simulation on the Kepler oscillator	41
7	Joint numerical simulation on the unit hypersphere and on the special orthogonal group	44
8	Proportional-integral-derivative control theory	48
8.1	Regulation of a second-order system by an M-PID controller . . .	49
8.2	Control efforts	51
8.3	Application of the general M-PID control theory to time-synchronization of second-order systems	52
9	Numerical simulations and experiments	55
9.1	Evaluation of the action of the cancelling component of the control field	57
9.2	Evaluation of the action of M-PID controllers on twin oscillators with identical reference points	59
10	Conclusion	70
A	Heun-like and Runge-like algorithms	75
A.1	Heun-like algorithm	75
A.2	Runge-like algorithm	77

Sommario

Questa tesi delinea una teoria di controllo non lineare, basata sullo schema di regolazione PID, per sincronizzare due sistemi dinamici di secondo ordine che insistono su una varietà Riemanniana. Inoltre, questo documento presenta alcune ricette numeriche per implementare i sistemi, così come lo schema di controllo, su una piattaforma di calcolo e un gran numero di risultati di simulazione numerica focalizzati sulla sincronizzazione di oscillatori non lineari tipo Duffing sulla sfera unitaria.

Abstract

This thesis outlines a non-linear control theory, based on the PID regulation scheme, to synchronize two second-order dynamical systems insisting on a Riemannian manifold. Also, this document presents some numerical recipes to implement the systems, as well as the control scheme, on a computing platform and a large number of numerical simulation results focused on the synchronization of Duffing-like non-linear oscillators on the unit sphere.

1. Introduction

Nonlinear dynamical systems on manifolds constitute a challenging and exciting research topic at the cross border of applied mathematics and theoretical sciences [4, 27]. Indeed, these dynamical systems have appeared in a number of subjects in pure mathematics as well as applied sciences [15, 21, 30]. Nonlinear dynamical systems on manifolds have been studied in the scientific literature because they arise naturally from the modeling of complex physical structures and because such dynamical systems constitute the basis for several modern applications. Such kind of dynamical systems are currently being investigated upon in at least two different contexts, according to their realm of application:

- **Synthetic (or algorithmic) systems:** These systems arise as extensions to manifold of classical nonlinear oscillators, such as the Duffing and the van Der Pol systems, or are designed specifically to generate complicated trajectories. These nonlinear systems are used to test non-linear signal processing algorithm and nonlinear control strategies, such as in the case of secure transmission of information by signal masking.
- **Models of physical phenomena:** These systems arise upon a modeling complicated physical phenomena, such as the rotational motion of a satellite or a drone and in general relativity.

The present paper focuses on synthetic nonlinear, second-order autonomous oscillators extended from flat Euclidean spaces to high-dimensional curved Riemannian manifolds and Lie groups in the manuscript [6]. In particular, the present contribution aims at exploring the rich dynamics of discrete-time nonlinear autonomous oscillators on manifolds and Lie groups and to exemplify their dynamics on two Riemannian manifolds of interest in the literature, namely, the unit-hypersphere and the special orthogonal group. The trajectories generated by such nonlinear dynamical systems evolve over time in complicated, possibly non-repeating, deterministic patterns.

From the perspective of the numerical simulation of dynamical systems on a computing platform, the chance of realizing numerical experiments is related to the availability of adequate numerical methods to approximate the trajectories generated by these dynamical systems. Classical numerical methods, such as the Euler method or the methods in the Runge-Kutta or Heun class, will fail if applied directly, as they are intrinsically designed to work on flat spaces and are not suitable to keep up with the non-flat shape of curved manifolds. These numerical methods may, however, be extended so as to cope with curved state manifolds by means of an expanding mathematical theory known as geometric integration. As a matter of fact, every dynamical system whose descriptive variables are bound to one another by nonlinear smooth constraints in such a way that their feasible states form a smooth manifold may be simulated numerically by means of the rich variety of mathematical tools provided by manifold calculus.

The behavior of these second-order dynamical systems is characterized in terms of scalar functions of motions, such as the kinetic energy, the potential energy and the total energy. The studied systems are also characterized as being either dissipative (i.e., damped) or conservative (i.e., non-damped). The potential energy function gives rise to the discussed variety of dynamical systems and the total energy, in the case of non-damped system, helps characterizing the quality of the numerical simulations.

Moreover, for what concerns synchronization of two dynamical systems, the general idea to control a dynamical system into approaching a desired state trajectory is to define an error field and to define an input signal as a linear combination of the error signal, of the time-derivative of the error signal and of a time-integral of the error. The vast majority of PID schemes [1] were developed to regulate dynamical systems whose input, state and output signals take values in a hyper-cube \mathbb{R}^n . The present document introduces a novel PID-inspired control theory for second-order dynamical systems whose state space is not a flat field but rather a *curved state manifold*, which will be referred to as M-PID regulation. Control of systems on state manifolds is a relatively new research branch in non-linear control theory which is gaining increasing interest especially in the field of mechanical systems regulation [2, 3, 17, 26].

In particular, in the present document we focus on a specific instance of non-linear control that affords the *synchronization* in time of the dynamics of two (either identical or non-identical) non-linear systems evolving on the same state manifold. Synchronization is a well-studied phenomenon that occurs spontaneously in nature when a large number of individuals are bound in a network [31], such as in a bird flock or within a heart muscle tissue. Synchronization of a leader-follower pair of dynamical systems found widespread applications in sciences and engineering as in secure transmission of information by signal masking [12] as well as in

humanoid robotics [22]. Even in this field, the large majority of synchronization techniques were developed taking as systems' state space the flat field \mathbb{R}^n . In the present research work, we shall be assuming that the state of the leader is accessible to the follower and that both states are accessible to the controller, although we assume that the leader state might be received upon being corrupted by noise (this is the case, for example, in brain cells networks [25]). Research works suggested that unavailability of accurate state measurements may be overcome by the help of Kalman filtering [11]. In this research work, we shall cope with synchronization of two second-order dynamical systems whose state spaces are curved state manifolds. The behavior of the devised M-PID-type time-synchronization theory will be illustrated through numerical experiments on two Duffing-type non-linear oscillators tailored to evolve on the unit hyper-sphere.

In order to simulate the behavior of non-linear dynamical systems on manifolds and of a control strategy on a computing platform, it is necessary to develop adequate numerical methods to approximate the trajectories generated by these dynamical systems and to compute the values of the control fields. Classical numerical methods, such as the Euler method or the Runge-Kutta class, will fail if applied directly, as they are intrinsically designed to work on flat spaces and are not suitable to keep up with the non-flat structure of curved manifolds. These numerical methods may, however, be extended so as to cope with curved state manifolds by means of numerical calculus on manifold [7, 8].

The present paper is organized as follows. Section 2 recalls dynamical systems on manifold and Lie groups. Section 3 illustrates the numerical resolution of second-order non-linear systems, examining in particular the forward Euler method, the Heun method and the Runge method. Section 4 shows potential energy functions of the abstract oscillators used on manifolds such as the simple pendulum, the Van der Pol oscillators, the Duffing-type oscillators and the Keplerian oscillators. Sections 5 and 6 illustrate the behavior of the introduced non-linear oscillators through numerical simulation on the unit hypersphere and on the special orthogonal group, respectively. Section 7 illustrates joint numerical simulation on both the unit hypersphere and the special orthogonal group. Section 8 recalls the classical proportional-integral-derivative control theory for second-order dynamical systems and presents an extension of such theory to manifolds (M-PID). Section 9 illustrates the devised M-PID-based synchronization algorithm by way of a number of numerical simulations and some applications to real cases. Section 10 concludes the document.

2. Dynamical systems on manifolds and Lie groups

The present section recalls some notation from manifold calculus and describes some kinds of dynamical systems on smooth manifolds and Lie groups.

2.1 Notation in manifold calculus

Let M denote a Riemannian manifold. At a point $x \in M$, the tangent space to the manifold M is denoted as $T_x M$. The symbol TM denotes the tangent bundle defined as $TM := \{(x, v) \mid x \in M, v \in T_x M\}$.

A Riemannian manifold M is endowed with a bilinear, positive-definite form $\langle \cdot, \cdot \rangle_x : T_x M \times T_x M \rightarrow \mathbb{R}$. A local metric $\langle \cdot, \cdot \rangle_x$ also defines a local norm $\|v\|_x := \sqrt{\langle v, v \rangle_x}$, for $v \in T_x M$.

The Riemannian gradient of a function $\psi : M \rightarrow \mathbb{R}$ evaluated at the point $x \in M$ is denoted as $\text{grad}_x \psi$. The covariant derivative of a vector field w in the direction of a vector $v \in T_x M$ is denoted as $\nabla_v w$. We assume M to be endowed with a *metric connection* (namely, that the covariant derivative of the metric tensor is identically zero) and the parallel transport operator $P^{x \rightarrow y}$ transports a tangent vector from $T_x M$ to $T_y M$.

A *manifold exponential* map $\exp : TM \rightarrow M$ applies as $\exp_x(v)$. Its inverse ‘log’ is defined only locally and is termed *manifold logarithm*. Given points $x, y \in M$, a manifold logarithm computes a tangent vector $v = \log_x(y) \in T_x M$ such that $\exp_x(v) = y$.

Given two points $x, y \in M$ connectable by a geodesic arc, their *Riemannian distance* is denoted by $d(x, y)$. On a Riemannian manifold, the distance between two nearby points may be evaluated by $d(x, y) = \|\log_x(y)\|_x$. A fundamental result of the calculus on manifolds states that the Riemannian gradient of a squared distance

function reads

$$\text{grad}_x d^2(x, y) = -2 \log_x(y), \quad (2.1)$$

wherever the logarithm is defined.

The covariant derivative of a vector field $w_x \in T_x M$ in the direction of a vector $v \in T_x M$ is denoted as $\nabla_v w$. We assume M to be endowed with a *metric connection* (namely, that the covariant derivative of the metric tensor is identically zero). The parallel transport operator $P^{x \rightarrow y}$ transports a tangent vector from $T_x M$ to $T_y M$. Parallel transport and covariant derivation are closely related to one another, in particular, covariant derivation may be expressed in terms of parallel transport as follows:

$$\nabla_v w = \lim_{h \rightarrow 0} \frac{P^{\gamma(h) \rightarrow x}[w_{\gamma(h)}] - w_x}{h}, \quad (2.2)$$

where γ denotes any smooth curve such that $\gamma(0) = x \in M$ and $\dot{\gamma}(0) = v \in T_x M$. Such relationship leads to a numerical approximation of the covariant derivative at a point x , namely

$$\nabla_v w \approx \frac{P^{\tilde{x} \rightarrow x}(w_{\tilde{x}}) - w_x}{h}, \quad (2.3)$$

where $\tilde{x} = \tilde{x}(x, h)$ denotes a point in M close to x .

2.2 Second-order dynamical systems on manifolds and Lie groups

The *kinetic energy function* $\mathcal{K} : TM \rightarrow \mathbb{R}$ for a dynamical system is defined by $\mathcal{K} := \frac{1}{2} \langle v, v \rangle_x$ for $(x, v) \in TM$. On a Riemannian manifold, the metric is positive-definite, hence, on every trajectory, it holds that $\mathcal{K} \geq 0$.

A *potential energy function* $\mathcal{V} : M \rightarrow \mathbb{R}$ depends on the coordinate $x \in M$ only. In absence of any external solicitation, the dynamical system generates a trajectory $x = x(t)$ that follows the landscape of the potential energy function.

The total energy \mathcal{H} of the dynamical system (2.5), is defined by:

$$\mathcal{H} := \mathcal{K} + \mathcal{V}. \quad (2.4)$$

Dynamical systems on manifolds. A general second-order dynamical system on a manifold M reads

$$\begin{cases} \dot{x} &= v, \\ \nabla_v v &= f(x, v, t), \end{cases} \quad (2.5)$$

in the tangent-bundle variables $(x(t), v(t)) \in TM$, where f denotes a forcing term, which may be composed as the sum of several contributions, like:

-
- *Friction-type damping (dissipative force)*: This kind of damping is expressed by the forcing term $-\mu \|v\|_x^{2(\varepsilon-1)} v$. Since, by definition, $\|v\|_x^2 = 2\mathcal{K}$, this kind of damping takes values $-\mu(2\mathcal{K})^{\varepsilon-1} v$.
 - *Conservative force*: It derives from the potential \mathcal{V} and reads $-\text{grad}_x \mathcal{V}$.

In the following, we shall only consider the two terms above, thus the dynamical system (2.5) assumes the expression:

$$\begin{cases} \dot{x} &= v, \\ \nabla_v v &= -\mu \|v\|_x^{2(\varepsilon-1)} v - \text{grad}_x \mathcal{V}. \end{cases} \quad (2.6)$$

It is straightforward to prove that the system (2.6) loses energy at a rate proportional to the kinetic energy. Only when $\mu = 0$ the dynamical system may retain its initial energy endlessly.

Lemma 2.2.1. *Over any trajectory of the dynamical system (2.6) the total energy either decreases or stay constant if $\mu = 0$.*

Proof. By manifold calculus, since the connection ∇ was assumed to be metric, we get:

$$\dot{\mathcal{H}} = \dot{\mathcal{V}} + \dot{\mathcal{K}} = \langle \text{grad}_x \mathcal{V}, \dot{x} \rangle_x + \langle v, \nabla_v v \rangle_x. \quad (2.7)$$

From the equations (2.6) it follows that

$$\dot{\mathcal{H}} = \langle \text{grad}_x \mathcal{V}, v \rangle_x + \langle v, -\mu \|v\|_x^{2(\varepsilon-1)} v - \text{grad}_x \mathcal{V} \rangle_x. \quad (2.8)$$

Therefore, from the bilinearity of the inner product and from the definition of the kinetic energy, it is readily concluded that

$$\dot{\mathcal{H}} = -\mu \|v\|_x^{2\varepsilon} = -\mu(2\mathcal{K})^\varepsilon \leq 0, \quad (2.9)$$

which proves the assertion. \square

It is interesting to discuss about the meaning of the asymptotic vanishing of the total energy to zero, in a damped system, in relation to the sign of the potential energy:

- **Definite potential energy function ($\mathcal{V} \geq 0$)**: Some dynamical systems are characterized by a potential energy function which takes exclusively non-negative values. Since the kinetic energy is always non-negative, in these systems, a vanishing total energy entails a vanishing kinetic and potential energy.

- **Indefinite potential energy function:** Those dynamical systems characterized by an indefinite potential energy function, which may take positive, null or negative values, exhibit a more interesting behavior. In fact, in these systems, a vanishing total energy does not necessarily correspond to a vanishing kinetic/potential energy. For instance, a damped system whose initial state is such that $\mathcal{H}(0) = 0$ will remain in a zero-energy state indefinitely, although the system may evolve while the potential energy of the system converts into kinetic energy, and vice-versa.

The indefiniteness of a continuous potential energy function entails the existence of a non-trivial *critical set*, defined as the point set $\mathbb{C} := \{x \in \mathbb{M} \mid \mathcal{V}(x) = 0\}$.

Dynamical systems on Lie groups. A special case of manifold is a Lie group, that is a manifold which carries over additional structure. A general second-order dynamical system on a manifold \mathbb{G} reads:

$$\begin{cases} \dot{X} &= X \cdot \Omega, \\ \dot{\Omega} &= f(X, \Omega, t), \end{cases} \quad (2.10)$$

in the trivialized tangent bundle variables $(X(t), \Omega(t)) \in \mathbb{G} \times \mathfrak{g}$. The notation $X \cdot$ is a short-hand for (inverse) left translation, which maps a tangent vector from the algebra \mathfrak{g} to the tangent space $T_X \mathbb{G}$. Here, f denotes again a forcing term (more like a mechanical torque, indeed), which may be composed as the sum of several contributions, like:

- *Friction-type damping (dissipative force):* This kind of damping is expressed by the forcing term $-\mu \|\Omega\|^{2(\varepsilon-1)} \Omega$. Here, $\|\cdot\|$ denotes a norm in the Lie algebra \mathfrak{g} .
- *Conservative force:* It derives from a potential \mathcal{V} and reads $-X^{-1} \cdot \text{grad}_X \mathcal{V}$. The notation $X^{-1} \cdot$ is a short-hand for left translation, which maps a tangent vector from the tangent space $T_X \mathbb{G}$ to the algebra \mathfrak{g} .

In the following, we shall only consider the two terms above, thus the dynamical system (2.10) assumes the expression:

$$\begin{cases} \dot{X} &= X \cdot \Omega, \\ \dot{\Omega} &= -\mu \|\Omega\|^{2(\varepsilon-1)} \Omega - X^{-1} \cdot \text{grad}_X \mathcal{V}. \end{cases} \quad (2.11)$$

For more details, see [6, 7].

3. Numerical simulation of second-order non-linear systems

The numerical methods for the approximate resolution of the differential equations of Subsection 2.2 are based on classical numerical schemes developed to simulate dynamical systems evolving in \mathbb{R}^n : we must therefore extend these equations to the case of a smooth manifold or a Lie group. The logic behind the implementation of these methods retraces the classical one, with the particular care to the fact that in a curved manifold, to advance a solution, it is unfeasible to add to the starting point the displacement that must be taken; instead, it is used the exponential map to perform a translation of the entity toward the desired direction. Subsection 3.1 recalls three classical numerical methods to solve initial-value problems, while Subsection 3.2 explains their extension to simulate second-order dynamical systems on manifolds.

3.1 Classical forward Euler, Heun and Runge methods

Let us recall that a first-order initial-value problem (IVP), to be solved numerically, reads:

$$\begin{cases} \dot{y}(t) &= f(y(t), t), t \geq 0, \\ y(0) &= y_0. \end{cases} \quad (3.1)$$

Let us recall and examine three numerical methods specifically:

- *Forward Euler method*: This is a first-order method, which means that the local error (error per step) is proportional to the square of the step size, and the global error (error at a given time) is proportional to the step size. Moreover, it can be said that for $h \rightarrow 0$, the approximate solution and the analytic one (which cannot always be obtained with the rules of differential calculus) will be coincident. However, not being able to choose h infinitely small, we will try to find an acceptably small value of h , below which the error, with

respect to the analytic solution, is acceptable. From a mathematical point of view, the procedure carried out is the following: from $dy/dt = f(y(t), t)$ and using an incremental rate approximation it can be written that:

$$\frac{y_{k+1} - y_k}{t_{k+1} - t_k} \approx f(y_k, t_k), \quad (3.2)$$

where $t_k := h \cdot k$ and y_k denotes a numerical approximation to the actual solution $y(t_k)$. Bringing y_{k+1} at first term:

$$y_{k+1} = y_k + hf(y_k, t_k), \quad (3.3)$$

where (3.3) will be called forward Euler method and $k = 0, 1, 2, \dots, .$

- *Heun's Method:* Heun's method may refer to the improved or modified Euler's method (that is, the explicit trapezoidal rule), or a similar two-stage Runge-Kutta method. The accuracy of the Euler method improves only linearly with the step size is decreased, whereas the Heun method improves accuracy quadratically. The scheme can be compared with the implicit trapezoidal method, but with $f(y_{k+1}, t_{k+1})$ replaced by $f(\tilde{y}_{k+1}, t_{k+1})$ in order to make it explicit. Here, \tilde{y}_{k+1} is the result of one step of forward Euler's method on the same initial value problem. Therefore, Heun's method is a predictor-corrector method with forward Euler's method as predictor and trapezoidal method as corrector. Let us start first of all from the expression in Crank-Nicolson:

$$y_{k+1} = y_k + h \frac{f(y_k, t_k) + f(y_{k+1}, t_{k+1})}{2},$$

that is an implicit method that requires the knowledge of the function at the point of arrival that is still unknown. Instead of y_{k+1} on the right-hand side, we will use the approximation: $\tilde{y}_{k+1} = y_k + hf(y_k, t_k)$, so it can be obtained that:

$$y_{k+1} = y_k + h \frac{f(y_k, t_k)}{2} + h \frac{f(y_k + hf(y_k, t_k), t_{k+1})}{2} \quad (3.4)$$

which can be rewritten more compactly by the classical Runge-Kutta notation as:

$$\begin{cases} \beta_{1,k} & := f(y_k, t_k), \\ \beta_{2,k} & := f(y_k + h\beta_{1,k}, t_{k+1}) \\ y_{n+1} & = y_n + \frac{h}{2}(\beta_{1,k} + \beta_{2,k}), \end{cases} \quad (3.5)$$

where the third formula of (3.5) is the Heun method, which belongs precisely to the class of the second order methods.

-
- *Runge's Method:* The RK2 method is also referred to as the midpoint method. Suppose to carry out a step with the explicit Euler method till half of the interval $t_{k+\frac{1}{2}} := t_k + \frac{h}{2}$, to calculate the value of the function $y_{k+\frac{1}{2}}$. Then, a complete step can be performed, in which the derivative is calculated in $t_{k+\frac{1}{2}}$ (that is, in the middle of the interval). Thus the Runge method is obtained:

$$y_{k+\frac{1}{2}} = y_k + h \frac{f(y_k, t_k)}{2}$$

and by replacing the above expression in $y_{k+1} = y_k + hf(y_{k+\frac{1}{2}}, t_{k+\frac{1}{2}})$, it can be obtained that:

$$y_{k+1} = y_k + hf(y_k + \frac{h}{2}f(y_k, t_k), t_k + \frac{h}{2}). \quad (3.6)$$

In the classical Runge-Kutta notation, the Runge method may be recast as a special case of the wide Runge-Kutta class of numerical methods by defining $\beta_{1,k} := f(y_k, t_k)$ and $\beta_{2,k} := f(y_k + ch\beta_{1,k}, t_k + bh)$. By this, the Runge's formula will be written as:

$$y_{k+1} = y_k + h(a_1\beta_{1,k} + a_2\beta_{2,k}).$$

Setting $a_1 := 0$ and $b, c := \frac{1}{2}$, it can be obtained that $\beta_{2,k} = f(y_k + \frac{h}{2}\beta_{1,k}, t_k + \frac{h}{2})$, therefore Runge's formula can be rewritten as:

$$y_{k+1} = y_k + h\beta_{2,k}. \quad (3.7)$$

3.2 Numerical simulation of second-order non-linear systems on manifolds by forward Euler, Heun and Runge techniques

This subsection extends the three numerical schemes recalled in the previous subsection to the case of a second-order dynamical system on a smooth manifold. In this subsection, we present a general scheme on a smooth manifold to solve the autonomous system of first-order equations on a tangent bundle TM :

$$\begin{cases} \dot{x} = f_x(x, v), \\ \nabla_v v = f_v(x, v), \end{cases} \quad (3.8)$$

where $f_x, f_v : TM \rightarrow TM$. Notice, in particular, that $f_x(x, v) \in T_xM$ and that $f_v(x, v) \in T_xM$, for $(x, v) \in TM$. Notice that the dynamical system (2.5) is a special

case of (3.8). Any extension of the previous methods to smooth manifolds needs to be carried out according to two general principles: 1) the dynamics (3.8) is described by two, first-order, coupled equations, therefore the Euler, Heun and the Runge methods need to get spliced in two parts; 2) the dynamics (3.8) takes place on the tangent bundle TM which is non-trivial (it trivializes to a flat space when $M = \mathbb{R}^n$).

Forward Euler method on manifold: According to the expressions of the geometric quantities of interest recalled above, a forward Euler method to achieve a discrete-time version of the dynamical system (3.8) reads:

$$\begin{cases} x_{k+1} &= \exp_{x_k}(h f_x(x_k, v_k)), \\ v_{k+1} &= \mathbf{P}^{x_k \rightarrow x_{k+1}}(v_k + h f_v(x_k, v_k)). \end{cases} \quad (3.9)$$

Heun method on manifold: A Heun method to achieve a discrete-time version of the dynamical system (3.8) reads:

$$\begin{cases} \beta_{1,k}^x &:= f_x(x_k, v_k), \text{ (Initial slope for } x) \\ \hat{x}_k &:= \exp_{x_k}(h \beta_{1,k}^x), \text{ (Aimed-to } x) \\ \beta_{1,k}^v &:= f_v(x_k, v_k), \text{ (Initial slope for } v) \\ \hat{v}_k &:= \mathbf{P}^{x_k \rightarrow \hat{x}_k}(v_k + h \beta_{1,k}^v), \text{ (Aimed-to } v) \\ \beta_{2,k}^x &:= f_x(\hat{x}_k, \hat{v}_k), \text{ (Final slope for } x) \\ \beta_{2,k}^v &:= f_v(\hat{x}_k, \hat{v}_k), \text{ (Final slope for } v) \\ x_{k+1} &= \exp_{x_k}\left(\frac{h}{2}(\beta_{1,k}^x + \mathbf{P}^{\hat{x}_k \rightarrow x_k}(\beta_{2,k}^x))\right), \\ v_{k+1} &= \mathbf{P}^{x_k \rightarrow x_{k+1}}\left(v_k + \frac{h}{2}(\beta_{1,k}^v + \mathbf{P}^{\hat{x}_k \rightarrow x_k}(\beta_{2,k}^v))\right). \end{cases} \quad (3.10)$$

Notice that the estimations of the slopes at the beginning/end of each interval are such that $\beta_{1,k}^x \in T_{x_k}M$, $\beta_{2,k}^x \in T_{\hat{x}_k}M$, $\beta_{1,k}^v \in T_{x_k}M$ and $\beta_{2,k}^v \in T_{\hat{x}_k}M$.

Runge method on manifold: A Runge method to achieve a discrete-time version of the dynamical system (3.8) reads:

$$\begin{cases} \beta_{1,k}^x &:= f_x(x_k, v_k), \text{ (Initial slope for } x) \\ \hat{x}_k &:= \exp_{x_k}\left(\frac{h}{2} \beta_{1,k}^x\right), \text{ (Aimed-to } x) \\ \beta_{1,k}^v &:= f_v(x_k, v_k), \text{ (Initial slope for } v) \\ \hat{v}_k &:= \mathbf{P}^{x_k \rightarrow \hat{x}_k}\left(v_k + \frac{h}{2} \beta_{1,k}^v\right), \text{ (Aimed-to } v) \\ \beta_{2,k}^x &:= f_x(\hat{x}_k, \hat{v}_k), \text{ (Midpoint slope for } x), \\ \beta_{2,k}^v &:= f_v(\hat{x}_k, \hat{v}_k), \text{ (Midpoint slope for } v), \\ x_{k+1} &= \exp_{x_k}\left(h \mathbf{P}^{\hat{x}_k \rightarrow x_k}(\beta_{2,k}^x)\right), \\ v_{k+1} &= \mathbf{P}^{x_k \rightarrow x_{k+1}}\left(v_k + h \mathbf{P}^{\hat{x}_k \rightarrow x_k}(\beta_{2,k}^v)\right). \end{cases} \quad (3.11)$$

The estimations of the slopes at the beginning/midpoint of each interval are such that $\beta_{1,k}^x, \beta_{1,k}^y \in T_{x_k} \mathbf{M}$, while $\beta_{2,k}^x, \beta_{2,k}^y \in T_{\hat{x}_k} \mathbf{M}$.

4. Potential energy functions and associated abstract oscillators on manifolds

The present section retraces some classical potential energy functions and extends them to a general Riemannian manifold. A similar discussion might be carried out about extensions of classical abstract systems to Lie groups, although one such discussion will be carried out directly through examples in the Section 6.

The ultimate purpose of defining and of extending potentials is to set up a consistent non-linear oscillator theory on manifolds. Non-linear oscillators find widespread applications in science and engineering. Examples are found in the design and implementation of a liquid mixing apparatus based on a stirring tank model [33], in the design of digital music synthesizers [28], in the design of haptic devices [32] and in secure transmission of information over digital networks by signal masking [8], where synchronization of non-linear oscillator is also a topic of prime interest, as it will be discussed later in this document.

4.1 Simple pendulum

A well-documented potential energy function is the one arising in the study of the simple pendulum. In the classical case that $M = \mathbb{R}$, it reads $\mathcal{V} \propto 1 - \cos x$, where x denotes the angular displacement from the equilibrium state. Such potential energy function may be extended to a general Riemannian manifold M , endowed with a Riemannian distance function $d(\cdot, \cdot)$, as:

$$\mathcal{V}^{(\text{pen})} := \kappa(1 - \cos d(x, r)), \quad (4.1)$$

with $\kappa > 0$ being a constant parameter and $r \in M$ denoting a reference point, which plays the role of an equilibrium state, in fact, the potential $\mathcal{V}^{(\text{pen})}$ presents

one of its minima in $x = r$. Rewrite the pendulum-type potential as $\mathcal{V}^{(\text{pen})} = \kappa - \kappa \cos(d^2(x, r))^{\frac{1}{2}}$. According to the calculation rule (2.1), its Riemannian gradient reads:

$$\text{grad}_x \mathcal{V}^{(\text{pen})} = -\kappa \frac{\sin d(x, r)}{d(x, r)} \log_x(r). \quad (4.2)$$

Notice that the above gradient is continuous in a neighborhood of r , in fact:

$$\lim_{x \rightarrow r} \frac{\sin d(x, r)}{d(x, r)} \log_x(r) = 0. \quad (4.3)$$

Also, it is worth noticing that the simple pendulum potential is always bounded by $0 \leq \mathcal{V}^{(\text{pen})} \leq 2\kappa$ even in the case that the distance function is not bounded (as it is the case for non-compact manifolds).

The dynamical system associated to the simple-pendulum potential reads:

$$\begin{cases} \dot{x} &= v, \\ \nabla_v v &= -\mu \|v\|_x^{2(\varepsilon-1)} v + \kappa \frac{\sin d(x, r)}{d(x, r)} \log_x(r). \end{cases} \quad (4.4)$$

4.2 Van der Pol oscillator

Balthazar Van der Pol was a Dutch electrical engineer who initiated modern experimental dynamics during the 1920's and 1930's. Van der Pol, first, introduced an equation to describe triode oscillations in electrical circuits [29]. The mathematical model for this system is a now well-known second order ordinary differential equation with cubic nonlinearity – the Van der Pol equation. The Van der Pol oscillator is a classical example of self-oscillatory system and is now considered as very useful mathematical model that can be used in much more complicated and modified systems. The potential energy function corresponding to the van der Pol dynamical system in the case $M = \mathbf{R}$ is a quadratic function, namely $\mathcal{V} \propto x^2$. Such potential energy function may be extended to a general Riemannian manifold M , endowed with a Riemannian distance function $d(\cdot, \cdot)$, as:

$$\mathcal{V}^{(\text{pol})} := \frac{1}{2} \kappa d^2(x, r), \quad (4.5)$$

with $\kappa > 0$ being a constant parameter and $r \in M$ denoting a reference point. The potential $\mathcal{V}_x^{(\text{pol})}$ presents its minimum in $x = r$. Its Riemannian gradient reads:

$$\text{grad}_x \mathcal{V}^{(\text{pol})} = -\kappa \log_x(r). \quad (4.6)$$

Therefore, the associated dynamical system reads:

$$\begin{cases} \dot{x} &= v, \\ \nabla_v v &= -\mu \|v\|_x^{2(\varepsilon-1)} v + \kappa \log_x(r). \end{cases} \quad (4.7)$$

4.3 Duffing-type oscillators

The Duffing oscillator, named after Georg Duffing, is a non-linear second-order differential equation used to model the motion of a damped oscillator with a more complex potential than in simple harmonic motion [13]. In physical terms, it models, for example, a spring pendulum whose spring's stiffness does not exactly obey Hooke's law. An extension of the Duffing potential reads:

$$\mathcal{V}^{(\text{duf})} := \pm \frac{1}{2}d^2(x, r) \pm \frac{1}{4}\kappa d^4(x, r), \quad (4.8)$$

where again $d(\cdot, \cdot)$ denotes the Riemannian (geodesic) distance on the manifold M , $\kappa > 0$ is a free parameter and $r \in M$ denotes a reference point. The signs \pm were introduced to account for the *soft* and the *double-well* Duffing oscillator. Let's distinguish the case that both addenda appear with the same sign or the case that the two addenda appear with opposite sign:

- If the Duffing potential is written as $\mathcal{V}_{++}^{(\text{duf})} = \frac{1}{2}d^2(x, r) + \frac{1}{4}\kappa d^4(x, r)$, then $\mathcal{V}_{++}^{(\text{duf})} \geq 0$, while if $\mathcal{V}_{--}^{(\text{duf})} = -\mathcal{V}_{++}^{(\text{duf})}$, then $\mathcal{V}_{--}^{(\text{duf})} \leq 0$ for any value of $x \in M$. In both cases, the point $x = r$ is the only point where the potential vanishes to zero and the only point of stationarity of the potential.
- If the Duffing potential is written as $\mathcal{V}_{+-}^{(\text{duf})} = \frac{1}{2}d^2(x, r) - \frac{1}{4}\kappa d^4(x, r)$ or as $\mathcal{V}_{-+}^{(\text{duf})} = -\mathcal{V}_{+-}^{(\text{duf})}$, then the Duffing potential may change sign according to the magnitude of the distance $d^2(x, r)$. In both cases, the point $x = r$ is not the only point where the potential vanishes to zero nor the only point of stationarity of the potential. In fact, by defining the critical distance $d_b := \sqrt{2/\kappa}$, it is immediate to see that at every point $x \in M$ such that $d(x, r) = d_b$ the potential changes sign.

Examples of Duffing potentials corresponding to different combinations of signs and different values of κ are illustrated in the Figure 4.1. The Riemannian gradient of Duffing potentials corresponding to different combinations of signs reads:

$$\text{grad}_x \mathcal{V}^{(\text{duf})} = [\mp 1 \mp \kappa d^2(x, r)] \log_x(r). \quad (4.9)$$

Apparently, the potential vanishes when $x = r$ but, in case of mixed signs, it also vanishes at every point $x \in M$ such that $d(x, r) = d_b$, therefore this system presents infinitely many critical points. Namely, we may define a set

$$\mathbb{C}^{(\text{duf})} := \left\{ x \in M \mid d(x, r) = \sqrt{2/\kappa} \right\} \quad (4.10)$$

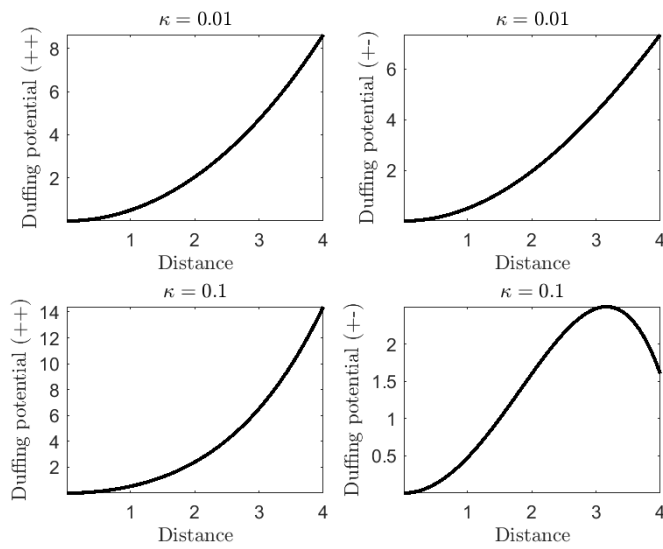


Figure 4.1: Example of Duffing potential corresponding to different combinations of signs and different values of κ . The (++) combination is referred to as hard Duffing potential while the combination (+-) is referred to as soft Duffing potential. (A combination (-+), not shown in the figure, is referred to as double-well potential.)

of critical points in M .

Therefore, the dynamical system associated to a Duffing potential reads:

$$\begin{cases} \dot{x} &= v, \\ \nabla_v v &= -\mu \|v\|_x^{2(\varepsilon-1)} v + \begin{cases} [1 + \kappa d^2(x, r)] \log_x(r), & \text{hard Duffing,} \\ [-1 - \kappa d^2(x, r)] \log_x(r), & \text{soft Duffing,} \\ [-1 + \kappa d^2(x, r)] \log_x(r), & \text{double-well Duffing.} \end{cases} \end{cases} \quad (4.11)$$

4.4 Keplerian oscillator

Likewise, a Keplerian (attractive-repulsive) potential [16] may be extended to a general Riemannian manifold M with Riemannian distance $d(\cdot, \cdot)$, by defining the Keplerian potential as:

$$\mathcal{V}^{(\text{kep})} := -\frac{\rho}{d(x, r)} + \lambda d(x, r), \quad (4.12)$$

with $\rho, \lambda > 0$. The Keplerian potential embodies a positive and a negative component. Indeed, upon defining a critical distance $d_c := \sqrt{\rho/\lambda}$, for which $\mathcal{V}^{(\text{kep})} = 0$, it is readily verified that if $d(x, r) < d_c$ then the negative component is prevailing, therefore $\mathcal{V}^{(\text{kep})} < 0$ and $|\mathcal{V}^{(\text{kep})}| \propto \frac{1}{d(x, r)}$, while if $d(x, r)$ is larger than the critical distance, the positive component prevails and the Keplerian potential is approximately linear in $d(x, r)$. An example of Keplerian potential with critical distance $d_c = 1$ is shown in the Figure 4.2.

Rewriting the Keplerian potential as $-\rho[d^2(x, r)]^{-\frac{1}{2}} + \lambda[d^2(x, r)]^{\frac{1}{2}}$ and invoking again the calculation rule (2.1), its Riemannian gradient reads:

$$\text{grad}_x \mathcal{V}^{(\text{kep})} = -\left[\frac{\rho}{d^3(x, r)} + \frac{\lambda}{d(x, r)} \right] \log_x(r). \quad (4.13)$$

The Riemannian gradient of the Keplerian potential does not describe a smooth vector field, since it presents a singularity at $x = r$. We observe that the Keplerian forcing term $-\text{grad}_x \mathcal{V}^{(\text{kep})}$ is always directed along the $\vec{x}\hat{r}$ directrix and that its amplitude is always non-vanishing, in fact

$$\left\| -\text{grad}_x \mathcal{V}^{(\text{kep})} \right\|_x = \left[\frac{\rho}{d^3(x, r)} + \frac{\lambda}{d(x, r)} \right] \|\log_x(r)\|_x = \lambda + \frac{\rho}{d^2(x, r)} > 0. \quad (4.14)$$

Moreover, for the Keplerian potential, we may define a set

$$\mathbb{C}^{(\text{kep})} := \left\{ x \in M \mid d(x, r) = \sqrt{\rho/\lambda} \right\} \quad (4.15)$$

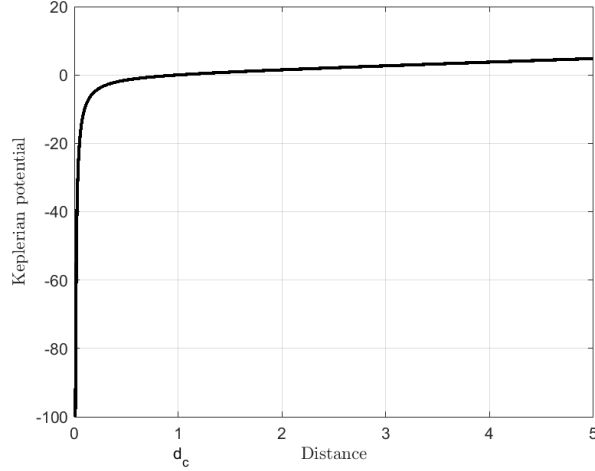


Figure 4.2: *Example of Keplerian potential with critical distance $d_c = 1$.*

of critical points in M .

The dynamical system associated to a Keplerian potential reads:

$$\begin{cases} \dot{x} &= v, \\ \nabla_v v &= -\mu \|v\|_x^{2(\varepsilon-1)} v + \left[\frac{\rho}{d^3(x,r)} + \frac{\lambda}{d(x,r)} \right] \log_x(r). \end{cases} \quad (4.16)$$

It is straightforward to envisage how all potential functions known in the physics literature based on distance functions may be extended to Riemannian manifolds on the basis of the Riemannian distance function. A well known example is the Lennard-Jones potential of computational chemistry or the electric/-gravitational potential.

5. Numerical simulation on the unit hypersphere

For the unit hypersphere \mathbb{S}^{n-1} endowed with the canonical metric $\langle w, v \rangle_x := w^\top v$, it holds that:

$$\begin{cases} d^2(x, y) = \arccos^2(x^\top y), \\ \mathbf{P}^{x \rightarrow y}(w) = \left[I_n - \frac{(I_n - xx^\top)yy^\top}{1 + x^\top y} - xy^\top \right] w, \\ \exp_x(v) = x \cos(\|v\|) + v \sin(\|v\|)/\|v\|, \\ \log_x(y) = (I_n - xx^\top)y((\sin d(x, y))/d(x, y))^{-1}. \end{cases} \quad (5.1)$$

where the symbol $\|\cdot\|$ denotes a vector 2-norm, the symbol I_n denotes a $n \times n$ identity matrix, the symbol $^\top$ denotes matrix transpose and $x \in \mathbb{S}^{n-1}$, $w, v \in T_x \mathbb{S}^{n-1}$. It is assumed that $x^\top y \neq -1$ in the expression of the parallel transport and that $v \neq 0$ in the expression of the exponential map.

Moreover an important fact to take into account in the numerical simulations is that the unit hypersphere is a compact manifold, therefore the distance function is bounded from above. In the case of the canonical metric, the upper bound is reached when two points $x, y \in \mathbb{S}^{n-1}$ are antipodal (namely, $x^\top y = -1$), hence $d_{\max} = \pi$. This fact also implies bounds on the values of the potential energy functions, which are based on the Riemannian distance.

In particular the unit sphere is the base manifold in a number of scientific and engineering problems. For examples, the unit sphere \mathbb{S}^2 plays an important role in robotics [10] as well as in quantum computation, where it represents the locus of pure quantum states $|\psi\rangle$ in a 1-qubit register (termed *Bloch sphere*, where the north pole represents $|0\rangle$ and the south pole represents the $|1\rangle$ bit) [18]. According to the expressions of the geometric quantities of interest recalled above, the discrete-time

version of the dynamical system (2.6) reads:

$$\begin{cases} x_{k+1} = x_k \cos(h\|v_k\|) + v_k \sin(h\|v_k\|)/\|v_k\|, \\ v_{k+1} = \mathbf{P}^{x_k \rightarrow x_{k+1}} [v_k - h\boldsymbol{\mu}(v_k^\top v_k)^{\varepsilon-1} v_k - h \operatorname{grad}_{x_k} \mathcal{V}], \end{cases} \quad (5.2)$$

with $h > 0$ being a discretization stepsize for the dynamical system and $k = 0, 1, 2, \dots$. Notice that $\varepsilon = 1$ corresponds to linear (viscous) damping.

5.1 Numerical simulation on the simple pendulum

The time-discretized version of the dynamical system (4.4) associated to the simple pendulum reads:

$$\begin{cases} x_{k+1} = x_k \cos(h\|v_k\|) + v_k \sin(h\|v_k\|)/\|v_k\|, \\ v_{k+1} = \mathbf{P}^{x_k \rightarrow x_{k+1}} \left[v_k - h\boldsymbol{\mu}(v_k^\top v_k)^{\varepsilon-1} v_k + h\boldsymbol{\kappa} \frac{\sin d(x_k, r)}{d(x_k, r)} (\mathbf{I}_n - x_k x_k^\top) r \left(\frac{\sin d(x_k, r)}{d(x_k, r)} \right)^{-1} \right], \end{cases} \quad (5.3)$$

with $h > 0$ being a discretization stepsize for the dynamical system and $\boldsymbol{\kappa} > 0$ is the coefficient of the pendulum potential, while ε is the exponential for nonlinear damping. Moreover, the system state is represented by the variable-pair $(x_k, v_k) \in T\mathbb{S}^{n-1}$ for any $k \in \mathbb{N}$. Notice that, as long as $x_k \neq r$, a cancellation occurs within the squared parentheses in the second equation, so that the discrete-time dynamical system may be re-expressed as

$$\begin{cases} x_{k+1} = x_k \cos(h\|v_k\|) + v_k \sin(h\|v_k\|)/\|v_k\|, \\ v_{k+1} = \mathbf{P}^{x_k \rightarrow x_{k+1}} [v_k - h\boldsymbol{\mu}(v_k^\top v_k)^{\varepsilon-1} v_k + h\boldsymbol{\kappa}(r - x_k(x_k^\top r))], \end{cases} \quad (5.4)$$

for $k = 0, 1, 2, \dots$. It is interesting to observe the emergence of an *effective damping coefficient* $\boldsymbol{\mu}^* := h\boldsymbol{\mu}$ and of an *effective potential coefficient* $\boldsymbol{\kappa}^* := h\boldsymbol{\kappa}$ which depend on the discretization stepsize. The values x_0 and v_0 denote the initial conditions of the systems. The potential energy function of the simple pendulum on the unit hypersphere is bounded as $0 \leq \mathcal{V}^{(\text{pen})} \leq 2\boldsymbol{\kappa}$. The simple pendulum on the sphere was simulated numerically in the presence as well as in the absence of a damping term.

The Figure 5.1 illustrates the behavior of a simple pendulum on the ordinary sphere \mathbb{S}^2 embedded in \mathbb{R}^3 in the absence of a damping term. The figure shows the trajectory generated by the dynamical system as well as the values of the potential, kinetic and total energy. In particular, the total energy \mathcal{H} , sum of potential and kinetic energies, should be preserved but it changes slightly due to numerical errors.

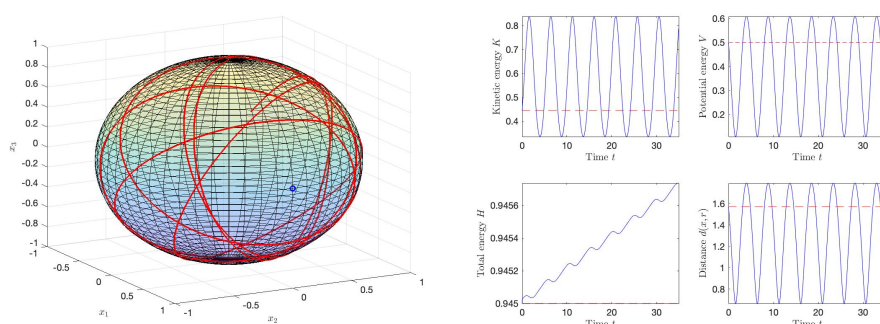


Figure 5.1: Behaviour of the simple pendulum (5.3) in the absence of non-linear damping (namely, $\mu = 0$). The left-hand side panel shows the trajectory in the space \mathbb{S}^2 , when the starting point is $x_0 = [0 \ 0 \ 1]^\top$, the reference point for the oscillator is $r = [1 \ 0 \ 0]^\top$ (denoted by a blue open circle) and the initial speed $v_0 = [0 \ -0.2 \ 0]^\top$. The parameters used in the simulation are $\kappa = 0.5$ and $h = 0.001$. The right-hand side panel shows the values taken by the kinetic energy, the potential energy and the total energy over the generated trajectory and the distance between the state x_k and the reference r . The red dashed lines represent the values of the shown quantities at the beginning of the numerical simulation (corresponding to the initial values x_0 and v_0).

Instead the Figure 5.2 illustrates the behavior of a simple pendulum on the ordinary sphere \mathbb{S}^2 embedded in \mathbb{R}^3 in the presence of a damping term. In this case the total energy tends asymptotically to zero due to damping.

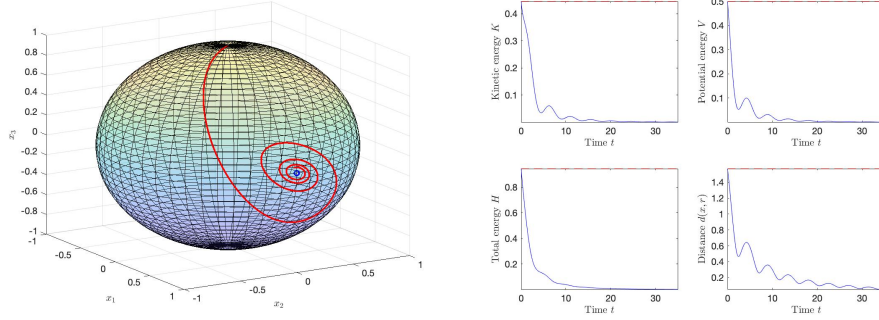


Figure 5.2: *Behaviour of the simple pendulum (5.3) in the presence of non-linear damping. The left-hand panel shows the trajectory in the space \mathbb{S}^2 , when the starting point is $x_0 = [0 \ 0 \ 1]^\top$, the reference point for the oscillator is $r = [1 \ 0 \ 0]^\top$ (denoted by a blue green circle) and the initial speed $v_0 = [0.5 \ -0.8 \ 0]^\top$. The parameters used in the simulation are $\kappa = 0.5$, $\mu = 0.5$, $\varepsilon = 1.3$ and $h = 0.002$.*

5.2 Numerical simulation on the hard Duffing oscillator

The time-discretized version of the dynamical system (4.11) associated to the hard Duffing potential reads:

$$\begin{cases} x_{k+1} = x_k \cos(h\|v_k\|) + v_k \sin(h\|v_k\|)/(\|v_k\|), \\ v_{k+1} = \mathbf{P}^{x_k \rightarrow x_{k+1}} [v_k - h\mu(v_k^\top v_k)^{\varepsilon-1} v_k + h(1 + \kappa d^2(x_k, r)) \log_{x_k}(r)]. \end{cases} \quad (5.5)$$

The hard Duffing oscillator on the sphere was simulated numerically in the presence as well as in the absence of a damping term.

The Figure 5.3 illustrates the behavior of a Duffing oscillator on the ordinary sphere \mathbb{S}^2 in the absence of a damping term. As expected, the state of this non-linear dynamical system oscillates around the reference point r . Moreover, the motion of the system continues endlessly due to the conservation of the total energy. Instead the Figure 5.4 illustrates the behavior of a hard Duffing oscillator on the ordinary sphere \mathbb{S}^2 in the presence of a damping term. In this case, the total energy of the system tends asymptotically to zero due to damping, hence the trajectory of the system spirals into the reference point.

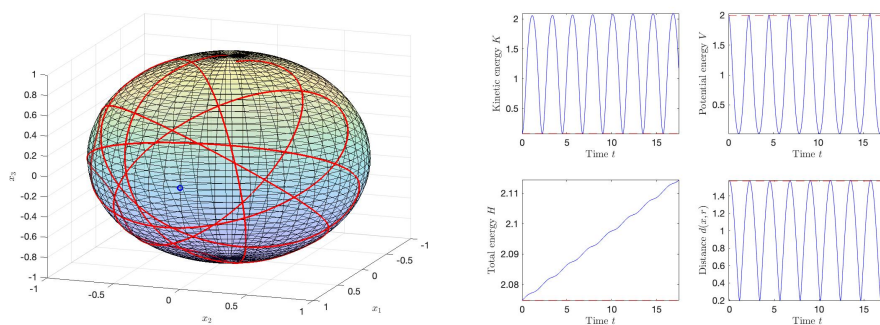


Figure 5.3: Behaviour of the hard Duffing (5.5) in the absence of non-linear damping (namely, $\mu = 0$). The left-hand side panel shows the trajectory in the space \mathbb{S}^2 , when the starting point is $x_0 = [0 \ 0 \ 1]^\top$, the reference point for the oscillator is $r = [1 \ 0 \ 0]^\top$ (denoted by a blue open circle) and the initial speed $v_0 = [0 \ -0.4 \ 0]^\top$. The parameters used in the simulation are $\kappa = 0.5$, $h = 0.0005$.

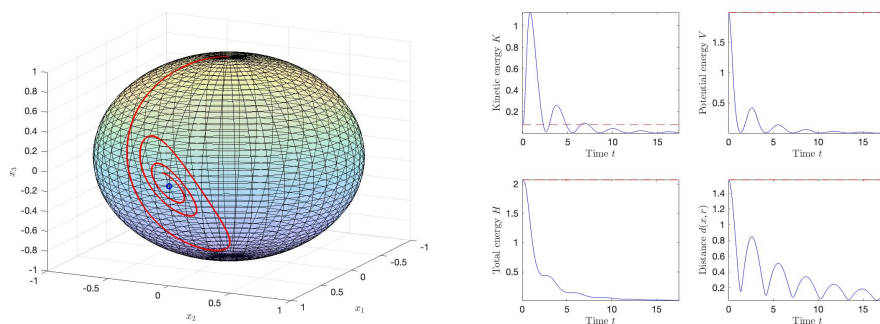


Figure 5.4: Behaviour of the hard Duffing (5.5) in the presence of non-linear damping. The left-hand panel shows the trajectory in the space \mathbb{S}^2 , when the starting point is $x_0 = [0 \ 0 \ 1]^\top$ the reference point for the oscillator is $r = [1 \ 0 \ 0]^\top$ (denoted by a green open circle) and the initial speed $v_0 = [0.5 \ -0.9 \ 0]^\top$. The parameters used in the simulation are $\kappa = 0.5$, $\mu = 0.5$, $\varepsilon = 1.3$ and $h = 0.001$.

5.3 Numerical simulation on the soft Duffing oscillator

In this case, starting from the equation (4.8), the potential corresponding to the soft Duffing oscillator reads:

$$\mathcal{V}^{(\text{duf})} := +\frac{1}{2}d^2(x, r) - \frac{1}{4}\kappa d^4(x, r), \quad (5.6)$$

and according to the calculation rule (4.9):

$$\text{grad}_x \mathcal{V}^{(\text{duf})} = (-1 + \kappa d^2(x, r)) \log_x(r). \quad (5.7)$$

This particular dynamical system has been implemented numerically by three different methods to be able to observe a better oscillation of kinetic and potential energies, a better conservation of total energy and to better evaluate the effects of the critical distance. Furthermore, two other methods called ‘‘Heun-like’’ and ‘‘RK2-like’’ have been implemented, based on the two classical methods used for first-order systems, see Appendix A.

5.3.1 Euler method

The time-discretized version of the dynamical system (4.11), implemented through the Euler method and associated to the soft Duffing potential reads:

$$\begin{cases} x_{k+1} = x_k \cos(h\|v_k\|) + v_k \sin(h\|v_k\|)/\|v_k\|, \\ v_{k+1} = \mathbf{P}^{x_k \rightarrow x_{k+1}} [v_k - h\mu(v_k^\top v_k)^{\varepsilon-1} v_k - h(-1 + \kappa d^2(x_k, r)) \log_{\mathbb{S}^2}(r)]. \end{cases} \quad (5.8)$$

The Figure 5.5 illustrates the behavior of a soft Duffing oscillator, implemented through the Euler method, on the ordinary sphere \mathbb{S}^2 in the absence of a damping term. As expected, the state of this non-linear dynamical system oscillates around the reference point r . Moreover, the motion of the system continues endlessly due to the conservation of the total energy.

The Figure 5.6 illustrates the behavior of a soft Duffing oscillator, implemented through the Euler method, on the ordinary sphere \mathbb{S}^2 in the presence of a damping term. In this case, the total energy of the system tends asymptotically to zero due to damping, hence the trajectory of the system spirals into the reference point.

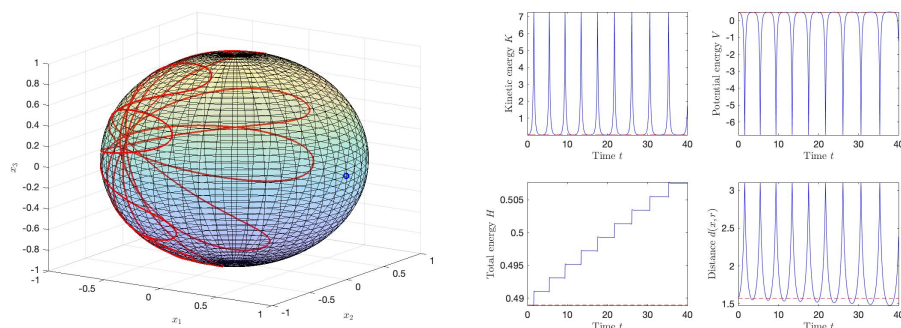


Figure 5.5: Behaviour of the soft Duffing (5.8) in the absence of non-linear damping (namely, $\mu = 0$), implemented through the Euler method. The left-hand side panel shows the trajectory in the space \mathbb{S}^2 , when the starting point is $x_0 = [0 \ 0 \ 1]^\top$, the reference point for the oscillator is $r = [1 \ 0 \ 0]^\top$ (denoted by a blue open circle) and the initial speed is $v_0 = [-1 \ -1.5 \ 0]^\top$. The parameters used in the simulation are $\kappa = 0.5$, $h = 0.0001$.

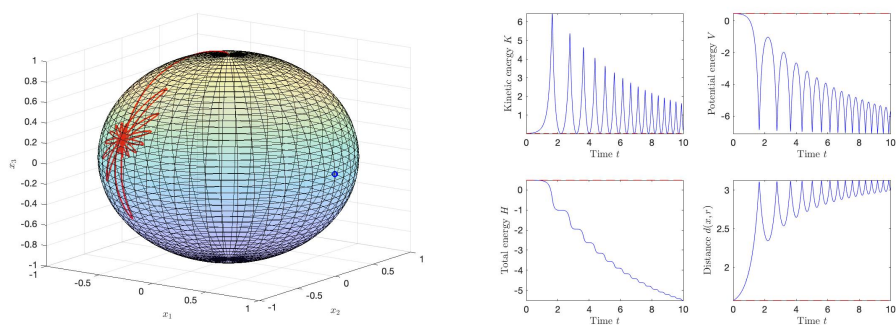


Figure 5.6: Behaviour of the soft Duffing (5.8) in the presence of non-linear damping, implemented through the Euler method. The left-hand panel shows the trajectory in the space \mathbb{S}^2 , when the starting point is $x_0 = [0 \ 0 \ 1]^\top$, the reference point for the oscillator is $r = [1 \ 0 \ 0]^\top$ (denoted by a blue open circle) and the initial speed $v_0 = [-1 \ -1.5 \ 0]^\top$. The parameters used in the simulation are $\kappa = 0.5$, $\mu = 0.2$, $\varepsilon = 1.3$ and $h = 0.0001$.

5.3.2 Heun method

The time-discretized version of the dynamical system (4.11), implemented through the Heun method described in (3.10), associated to the soft Duffing potential reads:

$$\begin{cases} \hat{x}_k := \exp_{x_k}(h v_k), \\ \beta_{1,k}^v := -\mu (v_k^\top v_k)^{\varepsilon-1} v_k - (-1 + \kappa d^2(x_k, r)) \log_{x_k}(r), \\ \hat{v}_k := \mathbf{P}^{x_k \rightarrow \hat{x}_k}(v_k + h \beta_{1,k}^v), \\ \beta_{2,k}^v := -\mu (\hat{v}_k^\top \hat{v}_k)^{\varepsilon-1} \hat{v}_k - (-1 + \kappa d^2(\hat{x}_k, r)) \log_{\hat{x}_k}(r), \\ x_{k+1} = \exp_{x_k}\left(h v_k + \frac{h^2}{2} \beta_{1,k}^v\right), \\ v_{k+1} = \mathbf{P}^{x_k \rightarrow x_{k+1}}\left[v_k + \frac{h}{2} \left(\beta_{1,k}^v + \mathbf{P}^{\hat{x}_k \rightarrow x_k}(\beta_{2,k}^v)\right)\right]. \end{cases} \quad (5.9)$$

The Figure 5.7 illustrates the behavior of a soft Duffing oscillator, implemented through the Heun method, on the ordinary sphere \mathbb{S}^2 in the absence of a damping term. As expected, the state of this non-linear dynamical system keeps oscillating around the reference point r .

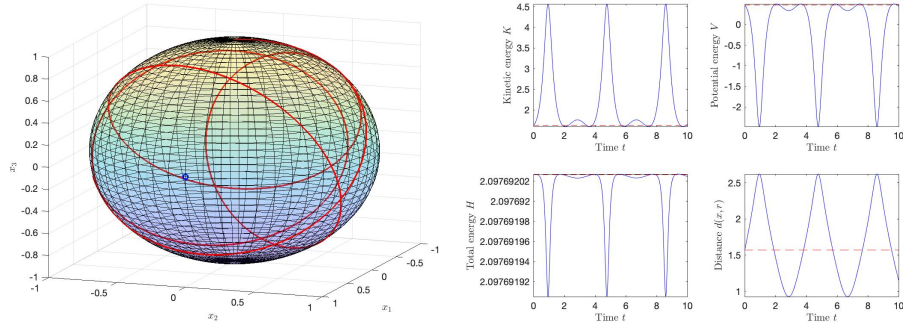


Figure 5.7: Behaviour of the soft Duffing (5.9) in the absence of non-linear damping (namely, $\mu = 0$), implemented through the Heun method. The left-hand side panel shows the trajectory in the space \mathbb{S}^2 , when the starting point is $x_0 = [0 \ 0 \ 1]^\top$, the reference point for the oscillator is $r = [1 \ 0 \ 0]^\top$ (denoted by a blue open circle) and the initial speed is $v_0 = [-1 \ -1.5 \ 0]^\top$. The parameters used in the simulation are $\kappa = 0.5$, $h = 0.0001$.

5.3.3 Runge (RK2) method

The time-discretized version of the dynamical system (4.11), implemented through the Runge method (3.11), associated to the soft Duffing potential reads:

$$\begin{cases} \hat{x}_k := \exp_{x_k} \left(\frac{h}{2} v_k \right), \\ \beta_{1,k}^v := -\mu (v_k^\top v_k)^{\varepsilon-1} v_k - (-1 + \kappa d^2(x_k, r)) \log_{x_k}(r), \\ \hat{v}_k := \mathbf{P}^{x_k \rightarrow \hat{x}_k} \left(v_k + \frac{h}{2} \beta_{1,k}^v \right), \\ \beta_{2,k}^v := -\mu (\hat{v}_k^\top \hat{v}_k)^{\varepsilon-1} \hat{v}_k - (-1 + \kappa d^2(\hat{x}_k, r)) \log_{\hat{x}_k}(r), \\ x_{k+1} = \exp_{x_k} \left(h v_k + \frac{h^2}{2} \beta_{1,k}^v \right), \\ v_{k+1} = \mathbf{P}^{x_k \rightarrow x_{k+1}} \left(v_k + h \mathbf{P}^{\hat{x}_k \rightarrow x_k}(\beta_{2,k}^v) \right). \end{cases} \quad (5.10)$$

where $k = 0, 1, 2, \dots$. It is worth underlining that, in general, the composition $\mathbf{P}^{x_k \rightarrow x_{k+1}} \circ \mathbf{P}^{\hat{x}_k \rightarrow x_k}$ does not coincide with $\mathbf{P}^{\hat{x}_k \rightarrow x_{k+1}}$, unless the points \hat{x}_k , x_k and x_{k+1} belong to the same geodesic arc. In practice, these points are pretty close to one another, therefore, in the context of a numerical stepping method, it would be feasible to replace the last step with $v_{k+1} = \mathbf{P}^{x_k \rightarrow x_{k+1}}(v_k) + h \mathbf{P}^{\hat{x}_k \rightarrow x_{k+1}}(\beta_{2,k}^v)$. Such approximation would save no computation, though!

The Figure 5.8 illustrates the behavior of a soft Duffing oscillator, implemented through the Runge method, on the ordinary sphere \mathbb{S}^2 in the absence of a damping term. As expected, the state of this non-linear dynamical system oscillates around the reference point r . The total energy is not exactly preserved by the Euler method.

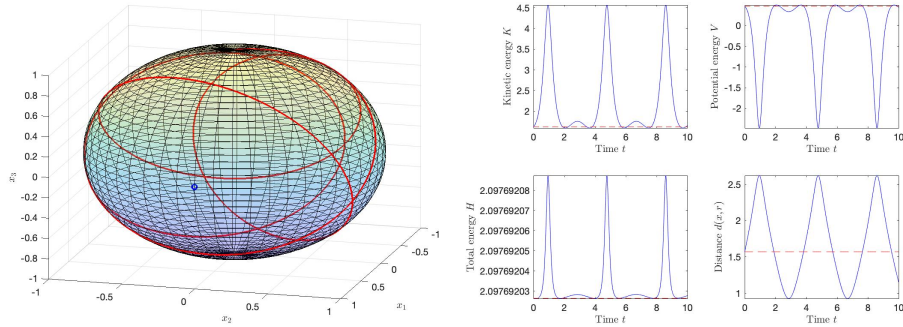


Figure 5.8: Behaviour of the soft Duffing (5.10) in the absence of non-linear damping (namely, $\mu = 0$), implemented through the Runge-Kutta method. The left-hand side panel shows the trajectory in the space \mathbb{S}^2 , when the starting point is $x_0 = [0 \ 0 \ 1]^\top$, the reference point for the oscillator is $r = [1 \ 0 \ 0]^\top$ (denoted by a blue open circle) and the initial speed is $v_0 = [-1 \ -1.5 \ 0]^\top$. The parameters used in the simulation are $\kappa = 0.5$, $h = 0.0001$.

It can be seen that by increasing the order of the method, the error becomes smaller

(in the Heun-based and Runge-based simulations, it is present in the tenth decimal digit). Therefore, it can be concluded that the fact that the total energy does not remain constant in the simulation made with Euler method is due to errors implicit in the method itself, and not to errors of code or formulas.

Moreover the Figures 5.5, 5.6, 5.7 and 5.8 show the relationship between the distance $d(x, r)$ and the potential energy $\mathcal{V}^{(\text{duf})}$, that is also interesting in this case. In fact, one can observe stationary points (local minima and maxima) of the potential energy:

- A local maximum of the distance $d(x, r)$ corresponds to a local minimum of potential energy $\mathcal{V}^{(\text{duf})}$.
- At a local minimum of distance $d(x, r)$ corresponds a local minimum of potential energy $\mathcal{V}^{(\text{duf})}$.

The critical distance value is $d_b \approx 2$. When the distance is smaller than the critical distance the potential energy becomes positive, while it is negative when the distance is larger than the critical distance. It can also be noted that in the soft Duffing case the repulsive action wins over the attractive one and therefore the oscillator tends to stabilize in the sphere at the farthest point from the reference.

5.4 Numerical simulation on the double-well Duffing oscillator

In this case, starting from the equation (4.8), the potential corresponding to the double-well Duffing oscillator reads:

$$\mathcal{V}^{(\text{duf})} := -\frac{1}{2}d^2(x, r) + \frac{1}{4}\kappa d^4(x, r), \quad (5.11)$$

and according to the calculation rule (4.9):

$$\text{grad}_x \mathcal{V}^{(\text{duf})} = (1 - \kappa d^2(x, r)) \log_x(r). \quad (5.12)$$

The time-discretized version of the dynamical system (4.11), implemented through the Euler method and associated to the double-well duffing potential reads:

$$\begin{cases} x_{k+1} = x_k \cos(h\|v_k\|) + v_k \sin(h\|v_k\|)/\|v_k\|, \\ v_{k+1} = \mathbf{P}^{x_k \rightarrow x_{k+1}} [v_k - h\mu(v_k^\top v_k)^{\varepsilon-1} v_k + h(-1 + \kappa d^2(x_k, r)) \log_{x_k}(r)]. \end{cases} \quad (5.13)$$

The Figure 5.9 illustrates the behavior of a double-well Duffing oscillator, implemented through the Euler method, on the ordinary sphere \mathbb{S}^2 in the absence of a damping term. As expected, the state of this non-linear dynamical system oscillates around the reference point r .

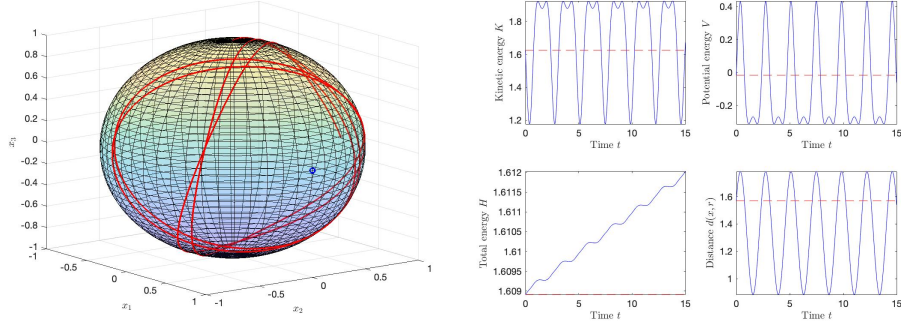


Figure 5.9: Behaviour of the double-well Duffing (5.13) in the absence of non-linear damping (namely, $\mu = 0$), implemented through the Euler method. The left-hand side panel shows the trajectory in the space \mathbb{S}^2 , when the starting point is $x_0 = [0 \ 0 \ 1]^\top$, the reference point for the oscillator is $r = [1 \ 0 \ 0]^\top$ (denoted by a blue open circle) and the initial speed is $v_0 = [-1 \ -1.5 \ 0]^\top$. The parameters used in the simulation are $\kappa = 0.8$, $h = 0.0001$.

The Figure 5.10 illustrates the behavior of a double-well Duffing oscillator, implemented through the Euler method, on the ordinary sphere \mathbb{S}^2 in the presence of a damping term. Moreover, the Figures 5.9 and 5.10 show the relationship between the distance $d(x, r)$ and the potential energy $\mathcal{V}^{(\text{duf})}$. In fact, there are stationary points of the potential energy:

- A local maximum of the distance $d(x, r)$ corresponds to a local maximum of potential energy $\mathcal{V}^{(\text{duf})}$.
- At a local minimum of distance $d(x, r)$ corresponds a local maximum of potential energy $\mathcal{V}^{(\text{duf})}$.

In the Figure 5.9, the critical distance is $d_b \approx 1.58$, while in the Figure 5.10, the critical distance is $d_b \approx 1.19$. When the distance is less than the critical distance the potential energy becomes negative, while it is positive when the distance is greater than the critical distance. Therefore we can observe a dual behavior with respect to the case of soft Duffing, due to the fact that they have the same potential and the same gradient, with opposite signs. It can also be noted that in the soft Duffing the repulsive action wins over the attractive one and therefore the oscillator tends to stabilize in the sphere at the point furthest from the reference. While in the double-well case, the attractive action wins, therefore the oscillator tends to stop in the reference point.

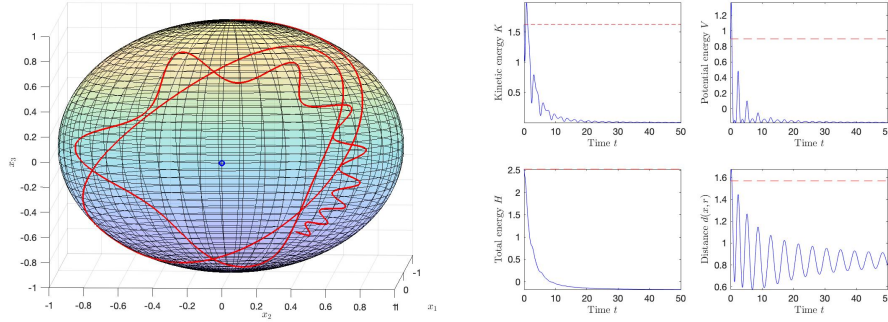


Figure 5.10: *Behaviour of the double-well Duffing (5.13) in the presence of non-linear damping, implemented through the Euler method. The left-hand panel shows the trajectory in the space \mathbb{S}^2 , when the starting point is $x_0 = [0 \ 0 \ 1]^\top$, the reference point for the oscillator is $r = [1 \ 0 \ 0]^\top$ (denoted by a blue open circle) and the initial speed $v_0 = [-1 \ -1.5 \ 0]^\top$. The parameters used in the simulation are $\kappa = 1.4$, $\mu = 0.2$, $\varepsilon = 1.3$ and $h = 0.0001$.*

5.5 Numerical simulation on the Van der Pol oscillator

On the basis of the general form of a second-order dynamical system on a manifold M (2.6), the time-discretized version of a dynamical system based on the van der Pol potential reads:

$$\begin{cases} x_{k+1} = x_k \cos(h\|v_k\|) + v_k \sin(h\|v_k\|)/\|v_k\|, \\ v_{k+1} = P^{x_k \rightarrow x_{k+1}} [v_k - h\mu(v_k^\top v_k)^{\varepsilon-1} v_k + h\kappa \log_{\mathbb{S}^k}(r)]. \end{cases} \quad (5.14)$$

Even in this case, it may be observed the emergence of an *effective damping coefficient* $\mu^* := h\mu$ and of an *effective potential coefficient* $\kappa^* := h\kappa$ which depend on the discretization stepsize.

The Figure 5.11 illustrates the behavior of a Van der Pol oscillator on the ordinary sphere \mathbb{S}^2 in the absence of a damping term. The total energy \mathcal{H} should keep constant, while a slight change is observable, which is solely due to numerical errors. The potential energy function of the van der Pol oscillator on the unit hypersphere is bounded as $0 \leq \mathcal{V}^{(\text{pol})} \leq \frac{1}{2}\kappa\pi^2$. Since, in this numerical simulation, $\kappa = 0.5$, the potential is bounded from above by $\mathcal{V}_{\max}^{(\text{pol})} \approx 2.47$. In fact, the potential values encountered in the simulations are well beyond such bound.

The Figure 5.12 illustrates the behavior of a Van der Pol on the ordinary sphere \mathbb{S}^2 embedded in \mathbb{R}^3 in the presence of a damping term. In this case, the system tends to loose its energy over time due to damping.

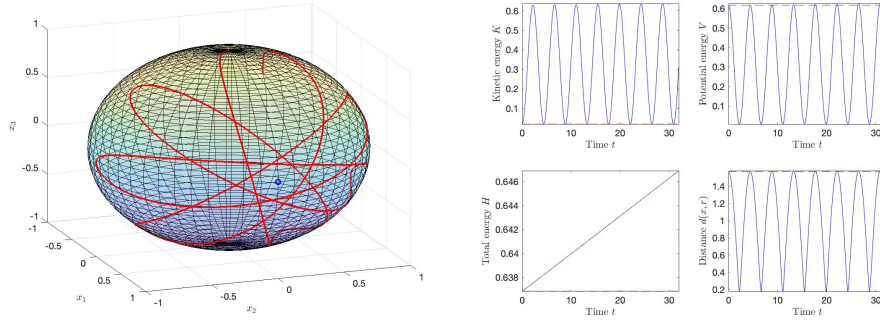


Figure 5.11: Behaviour of the Van der Pol oscillator (5.14) in the absence of non-linear damping (namely, $\mu = 0$). The left-hand side panel shows the trajectory in the space S^2 , when the starting point is $x_0 = [0 \ 0 \ 1]^\top$, the reference point for the oscillator is $r = [1 \ 0 \ 0]^\top$ (denoted by a blue open circle) and the initial speed $v_0 = [0 \ -0.2 \ 0]^\top$. The parameters used in the simulation are $\kappa = 0.5$ and $h = 0.001$.

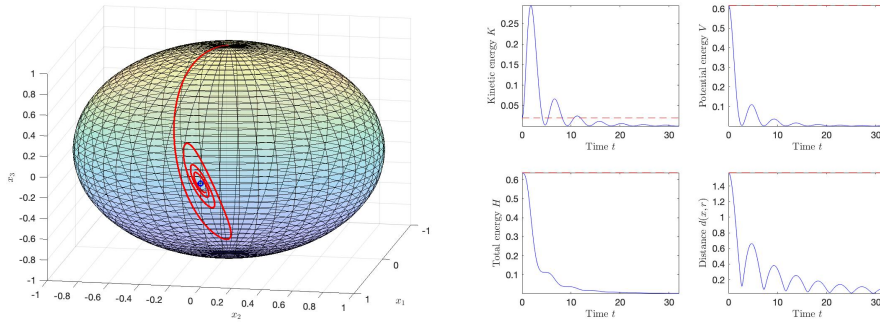


Figure 5.12: Behaviour of Van der Pol oscillator (5.14) in the presence of non-linear damping. The left-hand panel shows the trajectory in the space S^2 , when the starting point is $x_0 = [0 \ 0 \ 1]^\top$, the reference point for the oscillator is $r = [1 \ 0 \ 0]^\top$ (denoted by a blue open circle) and the initial speed $v_0 = [0.5 \ -0.9 \ 0]^\top$. The parameters used in the simulation are $\kappa = 0.5$, $\mu = 0.5$, $\varepsilon = 1.3$ and $h = 0.002$.

5.6 Numerical simulation on the Kepler oscillator

The time-discretized version of the dynamical system (4.16) associated to the simple pendulum reads:

$$\begin{cases} x_{k+1} = x_k \cos(h\|v_k\|) + v_k \sin(h\|v_k\|)/\|v_k\|, \\ v_{k+1} = \mathbf{P}^{x_k \rightarrow x_{k+1}} \left[v_k - h\boldsymbol{\mu}(v_k^\top v_k)^{\varepsilon-1} v_k + h \left(\frac{\rho}{d^3(x_k, r)} + \frac{\lambda}{d(x_k, r)} \right) \log_{x_k}(r) \right]. \end{cases} \quad (5.15)$$

Even in this case, it may be observed the emergence of an *effective damping coefficient* $\mu^* := h\boldsymbol{\mu}$ and of *effective potential coefficients* $\rho^* := h\rho$ and $\lambda^* := h\lambda$ which depend on the discretization stepsize. Notice that throwing in the expression of the logarithmic map and cancelling out an instance of distance, one gets the simplified expression:

$$\begin{cases} x_{k+1} = x_k \cos(h\|v_k\|) + v_k \sin(h\|v_k\|)/\|v_k\|, \\ v_{k+1} = \mathbf{P}^{x_k \rightarrow x_{k+1}} \left[v_k - h\boldsymbol{\mu}(v_k^\top v_k)^{\varepsilon-1} v_k + h \left(\lambda + \frac{\rho}{d^2(x_k, r)} \right) \frac{r - x_k(x_k^\top r)}{\sin d(x_k, r)} \right]. \end{cases} \quad (5.16)$$

The Figure 5.13 illustrates the behavior of a Kepler oscillator on the ordinary sphere \mathbb{S}^2 in the absence of any damping effect. In particular the total energy \mathcal{H} , sum of the potential energy and of the kinetic energy, should keep constant, while it changes slightly due to numerical errors. The potential energy is also proportional to the distance and, as we can see from the second and fourth graphs, always oscillates between a minimum and a maximum that remain constant. Furthermore, being in the presence of a maximum of potential energy means that it will be a minimum of kinetic energy due to the conservation of the total energy \mathcal{H} that should be preserved, although it changes slightly due to the accumulation of numerical errors.

The Figure 5.14 illustrates the behavior of a Kepler oscillator in the presence of a damping term. The energy curves illustrated in the Figure 5.14 show a phenomenon that never occurred in the previous numerical simulations. In fact, a continuous-time Kepler oscillator is expected to drive the state-variable x towards the reference point r , hence causing the value of the potential $\mathcal{V}^{(\text{kep})}$ to decrease indefinitely towards $-\infty$. In the numerical simulations performed by an Euler method, however, such expected behavior is not observed and the state-variable seems to stabilize in a circular orbit, around the reference point, of radius $d(x, r) \approx 0.14$. We recognized this phenomenon as a purely numerical artifact that tends to disappear as the value of the stepsize h decreases. For instance, taking $h = 0.00002$, the value of the radius decreases to approximately 0.01.

It can be seen that both in the damped and undamped case, if the distance is lesser than the critical distance, then the potential energy is negative, while if the

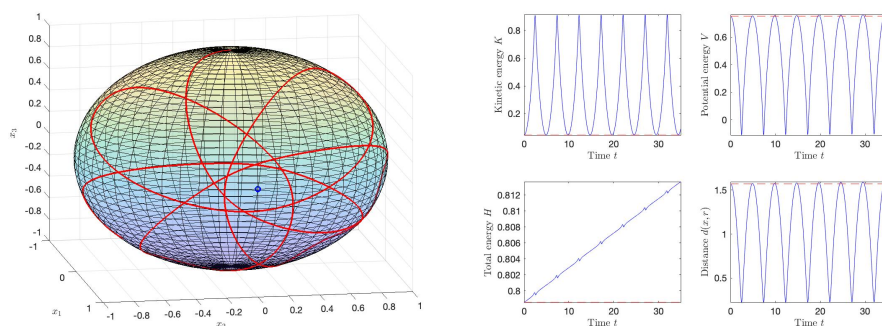


Figure 5.13: Behaviour of the Kepler oscillator (5.15) in the absence of non-linear damping (namely, $\mu = 0$). The left-hand side panel shows the trajectory in the space \mathbb{S}^2 , when the starting point is $x_0 = [0 \ 0 \ 1]^T$, the reference point for the oscillator is $r = [1 \ 0 \ 0]^T$ (denoted by a blue open circle) and the initial speed $v_0 = [0 \ -0.3 \ 0]^T$. The parameters used in the simulation are $\lambda = 0.5$, $\rho = 0.08$ and $h = 0.001$ (hence, the critical distance is $d_c = 0.4$).

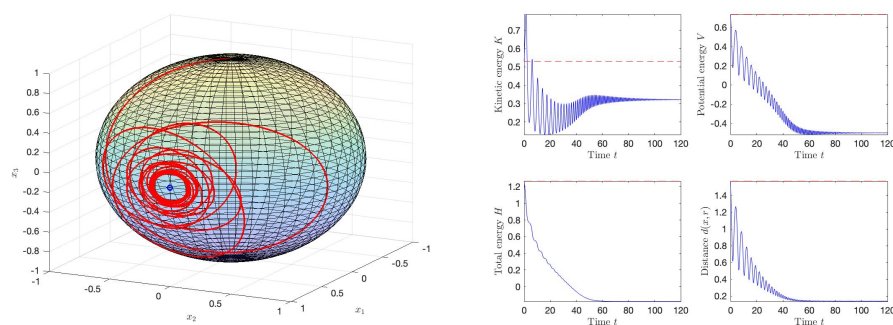


Figure 5.14: Behaviour of the Kepler oscillator (5.15) in the presence of non-linear damping. The left-hand panel shows the trajectory in the space \mathbb{S}^2 , when the starting point is $x_0 = [0 \ 0 \ 1]^T$, the reference point for the oscillator is $r = [1 \ 0 \ 0]^T$ (denoted by a blue open circle) and the initial speed $v_0 = [0.5 \ -0.9 \ 0]^T$. The parameters used in the simulation are $\rho = 0.08$, $\mu = 0.1$, $\varepsilon = 2$ and $\lambda = 0.5$ and $h = 0.002$ (hence, the critical distance is $d_c = 0.4$).

distance is larger than the critical one, the potential energy is positive.

6. Numerical simulation on the special orthogonal group $\text{SO}(3)$

For the special orthogonal group $\text{SO}(3)$ endowed with the canonical metric $\langle W, V \rangle_x := \text{tr}(W^T V)$, it holds that:

$$\begin{cases} d^2(X, Y) = -\text{tr}[\text{Log}^2(X^T Y)], \\ \exp_X(V) = X \text{Exp}(X^T V), \\ \log_X(Y) = X \text{Log}(X^T Y), \end{cases} \quad (6.1)$$

where $X, Y \in \text{SO}(3), V \in T_X \text{SO}(3) := \{X\Omega \mid \Omega \in \mathfrak{so}(3)\}$, with $\mathfrak{so}(3) := \{\Omega \in \mathbb{R}^{3 \times 3} \mid \Omega^T + \Omega = 0\}$. Moreover, the symbols Exp and Log denote the matrix exponential and the principal matrix logarithm, respectively. The matrix logarithm was implemented using a special numerical recipe based on a Schur decomposition, explained in [24]. The kinetic energy for the dynamical systems in this section takes the expression $\mathcal{K} = -\frac{1}{2} \text{tr}[\Omega^2]$, where $\Omega \in \mathfrak{so}(3)$ denotes the system's angular speed matrix. According to the expressions of the geometric quantities of interest recalled above, the discrete-time version of the dynamical system (2.11) reads:

$$\begin{cases} X_{k+1} = X_k \text{Exp}(h\Omega_k), \\ \Omega_{k+1} = (1 - h\mu \|\Omega_k\|^{2(\varepsilon-1)})\Omega_k - hX_k^T \text{grad}_{X_k} \mathcal{V}, \end{cases} \quad (6.2)$$

with $h > 0$ being a discretization stepsize for the dynamical system and $\varepsilon > 0$ being the exponential for nonlinear damping. The system state is represented by the pair $(X_k, \Omega_k) \in \text{SO}(3) \times \mathfrak{so}(3)$ for $k \in \mathbb{N}$. The first equation of the numerical method (6.2) represents a geodesic-based Euler-like step-forward numerical approximation of the flow associated with the first differential equation on the tangent bundle $T\text{SO}(3)$. The second equation represents a direct Euler-like step-forward method that takes place on a linear space, namely, the Lie algebra $\mathfrak{so}(3)$.

6.1 Visual rendering via a group action on a manifold

In order to achieve visual rendering of the $\text{SO}(3)$ -trajectories generated by the non-linear oscillators, we shall be exploiting the notion of group action on a manifold. Given a group \mathbb{G} and a smooth manifold M , a *group action* $\Lambda : \mathbb{G} \times M \rightarrow M$ is denoted as $y = \Lambda_g(x)$, where $g \in \mathbb{G}$ and $x, y \in M$ [5]. It is worth recalling that an *orbit* of a point $x \in M$ under a group action Λ is defined as $\mathbb{G}^\Lambda \cdot x := \{\Lambda_g(x) \mid g \in \mathbb{G}\}$ [5]. In the case of interest in the present report, a suitable group action is invoked in order to provide a 3-dimensional graphical rendering of trajectories generated in the Lie group of 3-dimensional rotations, which are represented by 3×3 matrices. Therefore, we take $\mathbb{G} = \text{SO}(3)$ and $M = \mathbb{S}^2$ and define $\Lambda_X(p) := Xp$, with $X \in \text{SO}(3)$ and $p \in \mathbb{S}^2$. Clearly, a trajectory will be represented as a subset of $\text{SO}(3)^\Lambda \cdot p \cong \mathbb{S}^2$.

In other words, in the numerical simulations, the trajectories generated by the oscillators have been represented in the hyper-sphere \mathbb{S}^2 . In particular, taken an arbitrary ‘seed’ on the hyper-sphere, it is multiplied by the initial rotation matrix, belonging to $\text{SO}(3)$. Also the reference point is obtained multiplying the starting point by the reference rotation matrix. Therefore, in this way, the starting vector assumes an initial inclination and it will oscillate around a reference inclination. Only in the non-damped case (when $\mu = 0$) the reference inclination matrix is taken randomly, because in this way, better trajectories are obtained during the simulations. As the inclination matrix evolves over time, it will change its value according to the laws of the considered oscillator. So, multiplying this matrix by the initial vector belonging to \mathbb{S}^2 , we will obtain, instant by instant, a vector that will belong to the sphere with a new inclination.

6.2 Numerical simulation on the simple pendulum

In this instance of a dynamical system on the manifold $\text{SO}(3)$, the potential energy function takes the expression $\mathcal{V}^{(\text{pen})} := \kappa \left(1 - \cos \left(\sqrt{-\text{tr} [\text{Log}^2(X^\top R)]} \right) \right)$, where $X \in \text{SO}(3)$ denotes the system’s orientation state matrix and $R \in \text{SO}(3)$ denotes a reference point for the system’s oscillations. The time-discretized version of the dynamical system (4.4) on the manifold of special orthogonal matrices, associated to the simple pendulum, reads:

$$\begin{cases} X_{k+1} = X_k \text{Exp}(h\Omega_k), \\ \Omega_{k+1} = (1 + h\mu \text{tr}[\Omega_k^2]^{\varepsilon-1})\Omega_k + h\kappa \frac{\sin d(X_k, R)}{d(X_k, R)} \text{Log}(X_k^\top R), \end{cases} \quad (6.3)$$

with $h > 0$ being a discretization stepsize for the dynamical system and $k = 0, 1, 2, \dots$, $\mu, \varepsilon > 0$ being coefficients of the nonlinear damping term and $\kappa > 0$

being a coefficient for the potential.

The Figure 6.1 illustrates the behavior of a simple pendulum on the special orthogonal group $SO(3)$ embedded in R^3 in the absence of a damping term. Notice again how the total energy \mathcal{H} should be preserved, although it changes slightly due to numerical errors introduced by the numerical method.

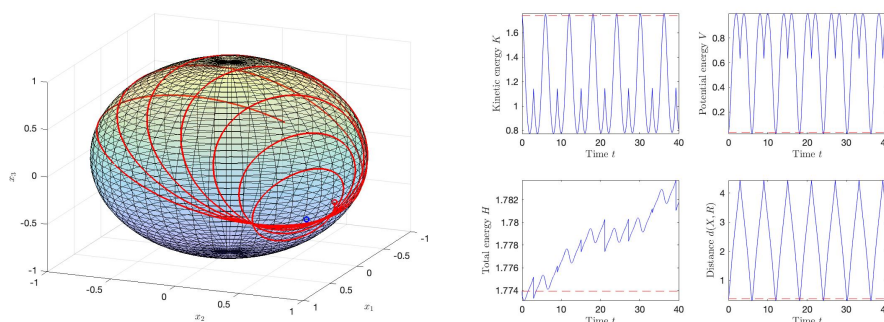


Figure 6.1: *Behaviour of the classic pendulum oscillator (6.3) on the special orthogonal group $SO(3)$, in the absence of non-linear damping (namely, $\mu = 0$). The left-hand side panel shows the trajectory in the space S^2 , when the starting point and also the reference point are taken randomly, (denoted by a blue open circle) and the initial speed will be random, because related to the initial state. The parameters used in the simulation are $\kappa = 0.5$ and $h = 0.002$.*

The Figure 6.2 illustrates the behavior of a single pendulum oscillator on the special orthogonal group $SO(3)$ embedded in R^3 in the presence of a damping term. In this case, the total energy of the system tends asymptotically to zero due to damping.

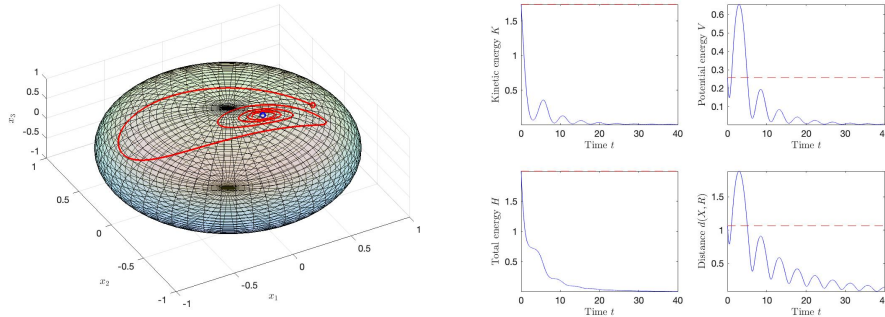


Figure 6.2: Behaviour of the simple pendulum (6.3) in the presence of non-linear damping. The left-hand panel shows the trajectory on the special orthogonal group $SO(3)$, when the starting point and also the reference point are taken randomly (denoted by a blue open circle) the initial speed will be random, because related to the initial state. The parameters used in the simulation are $\kappa = 0.5$, $\mu = 0.3$, $\varepsilon = 1.3$ and $h = 0.002$.

6.3 Numerical simulation on a hard Duffing oscillator

In this instance of a dynamical system on the Lie group $SO(3)$, the potential energy function takes the expression $\mathcal{V}^{(\text{duf})} := \mp \frac{1}{2} \text{tr} [\text{Log}^2(X^\top R)] \pm \frac{1}{4} \kappa \text{tr} [\text{Log}^2(X^\top R)]^2$, where $X \in SO(3)$ denotes the system's orientation state matrix and $R \in SO(3)$ denotes a reference point for the system's oscillations. Since the potential is a quartic form in the Riemannian distance (but not in the system's state), the potential might be referred to as *quartic*.

The time-discretized version of the dynamical system (4.11) on the manifold of special orthogonal matrices, associated to the hard Duffing oscillators, reads:

$$\begin{cases} X_{k+1} = X_k \text{Exp}(h\Omega_k), \\ \Omega_{k+1} = (1 + h\mu \text{tr}[\Omega_k^2]^{\varepsilon-1})\Omega_k + h(1 + \kappa d^2(X_k, R)) \text{Log}(X_k^\top R). \end{cases} \quad (6.4)$$

The Figure 6.3 illustrates the behavior of a hard Duffing oscillator on the special orthogonal group $SO(3)$ embedded in \mathbb{R}^3 in the absence of a damping term via a Lie-group action-based rendering technique.

The Figure 6.4 illustrates the behavior of a hard Duffing oscillator on the special orthogonal group $SO(3)$ embedded in \mathbb{R}^3 in the presence of a damping term.

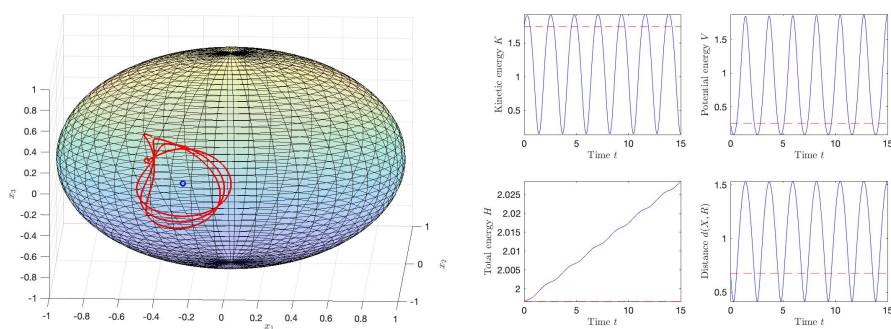


Figure 6.3: Behaviour of a hard Duffing oscillator (6.4) on the special orthogonal group $SO(3)$, in the absence of non-linear damping (namely, $\mu = 0$). The left-hand side panel shows the trajectory on the special orthogonal group $SO(3)$, when the starting point and also the reference point are taken randomly, (denoted by a blue open circle) and the initial speed will be random, because related to the initial state. The parameters used in the simulation are $\kappa = 0.5$ and $h = 0.0005$.

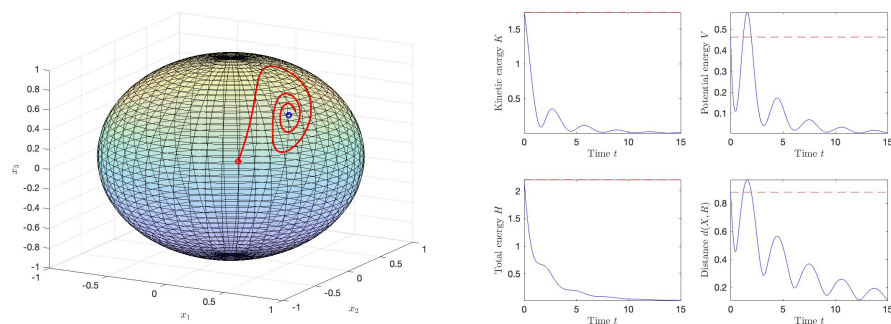


Figure 6.4: Behaviour of a hard Duffing oscillator (6.4) in the presence of non-linear damping. The left-hand panel shows the trajectory in the special orthogonal group $SO(3)$, when the starting point and also the reference point are taken randomly (denoted by a blue open circle) the initial speed will be random, because related to the initial state. The parameters used in the simulation are $\kappa = 0.5$, $\mu = 0.5$, $\varepsilon = 1.3$ and $h = 0.0008$.

6.4 Numerical simulation on the Var der Pol oscillator

In this instance of a dynamical system on the manifold $SO(3)$, the potential energy function takes the expression $\mathcal{V}^{(\text{pol})} = -\frac{1}{2} \kappa \text{tr}[\text{Log}^2(X^\top R)]$, where $X \in SO(3)$ denotes the system's orientation state matrix and $R \in SO(3)$ denotes a reference point for the system's oscillations. Since the potential is a quadratic form in the Riemannian distance (but not in the system's state), the potential might be referred to as *quadratic*.

The time-discretized version of the dynamical system (4.7) on the manifold of special orthogonal matrices, associated to the Van der Pol oscillator, reads:

$$\begin{cases} X_{k+1} = X_k \text{Exp}(h\Omega_k), \\ \Omega_{k+1} = (1 + h\mu \text{tr}[\Omega_k^2] \varepsilon^{-1}) \Omega_k + h\kappa \text{Log}(X_k^\top R). \end{cases} \quad (6.5)$$

The Figure 6.5 illustrates the behavior of a Van der Pol oscillator on the special orthogonal group $SO(3)$ in the absence of a damping term.

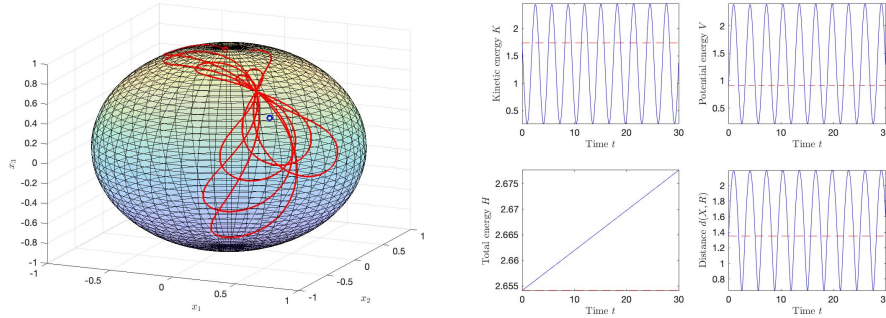


Figure 6.5: *Behaviour of the Van der Pol oscillator (6.5) on the special orthogonal group $SO(3)$, in the absence of non-linear damping (namely, $\mu = 0$). The left-hand side panel shows the trajectory in the space \mathbb{S}^2 , when the initial point and also the reference point are taken randomly, (denoted by a blue open circle) and the initial speed will be random, because related to the initial state. The parameters used in the simulation are $\kappa = 1$ and $h = 0.0005$.*

Instead the Figure 6.6 illustrates the behavior of a Van der Pol oscillator on the special orthogonal group $SO(3)$ in the presence of a damping term.

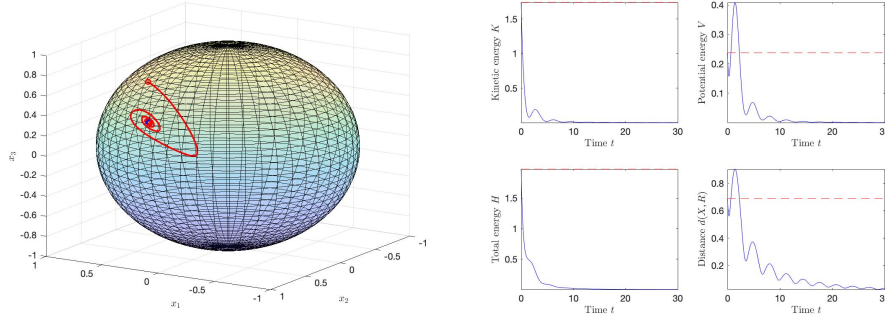


Figure 6.6: Behaviour of the Van der Pol (6.5) in the presence of non-linear damping. The left-hand panel shows the trajectory in the special orthogonal group $SO(3)$, when the initial point and also the reference point are taken randomly (denoted by a blue open circle) the initial speed will be random, because related to the initial state. The parameters used in the simulation are $\kappa = 1$, $\mu = 0.5$, $\varepsilon = 3$ and $h = 0.001$.

6.5 Numerical simulation on the Kepler oscillator

In this instance of a dynamical system on the manifold $SO(3)$, the potential energy function takes the expression $\mathcal{V}^{(\text{kep})} := -\rho/d(X, R) + \lambda d(X, R)$, where $X \in SO(3)$ denotes the system's orientation state matrix and $R \in SO(3)$ denotes a reference point for the system's oscillations.

The time-discretized version of the dynamical system (4.16) on the group-manifold of special orthogonal matrices, associated to the Kepler oscillator, reads:

$$\begin{cases} X_{k+1} = X_k \text{Exp}(h\Omega_k), \\ \Omega_{k+1} = (1 + h\mu \text{tr}[\Omega_k^2]^{\varepsilon-1})\Omega_k + h\left(\frac{\rho}{d^3(X_k, R)} + \frac{\lambda}{d(X_k, R)}\right) \text{Log}(X_k^\top R). \end{cases} \quad (6.6)$$

The Figure 6.7 illustrates the behavior of a Kepler oscillator on the special orthogonal group $SO(3)$ in the absence of a damping term.

Instead the Figure 6.8 illustrates the behavior of a Kepler oscillator on the special orthogonal group $SO(3)$ in the presence of a damping term. It is interesting to notice that the kinetic energy does not tend to zero, which indicates that this dynamical system keeps oscillating. Remembering from the consideration (4.12), if $d(x, r) < d_c$ (where $d_c \approx 0.45$) the negative component becomes greater than the positive one and the potential energy became $\mathcal{V}^{(\text{kep})} \leq 0$, thus it decreases. Therefore, the distance vanishes to zero, namely the reference point is reached, even though the kinetic energy and the total energy do not vanish to zero. It can be seen

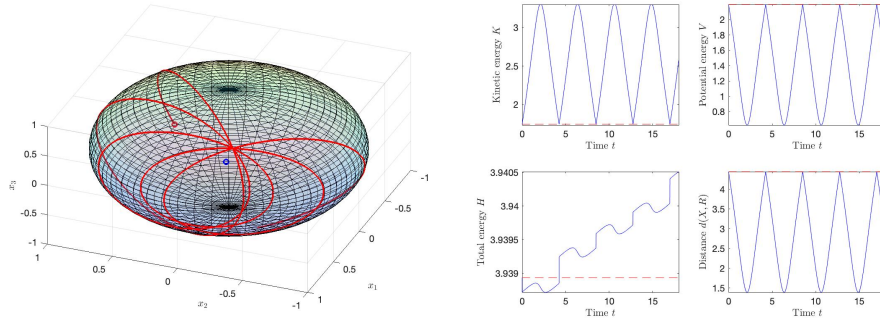


Figure 6.7: Behaviour of the Kepler oscillator (6.6) on the special orthogonal group $SO(3)$, in the absence of non-linear damping (namely, $\mu = 0$). The left-hand side panel shows the trajectory in the space \mathbb{S}^2 , when the starting point and also the reference point are taken randomly, (denoted by a blue open circle) and the initial speed will be random, because related to the initial state. The parameters used in the simulation are $\lambda = 0.2$, $\rho = 0.8$ and $h = 0.0003$.

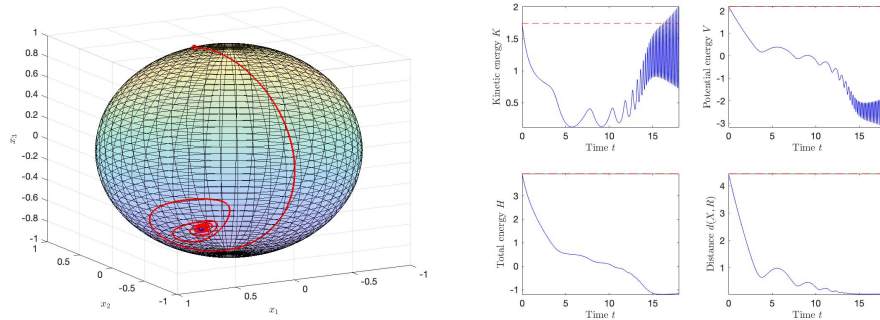


Figure 6.8: Behaviour of the Kepler oscillator (6.6) in the presence of non-linear damping. The left-hand panel shows the trajectory on the special orthogonal group $SO(3)$, when the starting point and also the reference point are taken randomly (denoted by a blue open circle) the initial speed will be random, because related to the initial state. The parameters used in the simulation are $\lambda = 0.5$, $\mu = 0.3$, $\rho = 0.1$, $\varepsilon = 1.5$ and $h = 0.0003$.

that both in the damped and undamped case if the distance is less than the critical distance, then the potential energy is negative, while if the distance is greater than the critical one, the potential energy is positive.

7. Joint numerical simulation on the unit hypersphere and on the special orthogonal group

This simulation shows the behavior of a rigid body (a ‘cube’) whose center of mass lays on the sphere \mathbb{S}^2 and its position changes according to the trajectory generated by a \mathbb{S}^2 -oscillator, while its instantaneous orientation changes according to a rotation sequence generated by a $\text{SO}(3)$ -oscillator. The combination of the two motions will result in a body translating and rotating in the unit sphere with a defined oscillation. In the simulation, a classical pendulum oscillator (4.4) both for the position and for the orientation was chosen.

The Figure 7.1 illustrates the behavior of a classical pendulum that oscillates on the hyper-sphere \mathbb{S}^2 and on the special orthogonal group $\text{SO}(3)$. The two oscillators are not damped, therefore they will oscillate around the reference point on the hypersphere and around their reference inclination, indefinitely.

The parameters used in the simulation are $\kappa = 0.5$ and $h = 0.001$. Moreover in \mathbb{S}^2 the initial position point is $x_0 = [0 \ 0 \ 1]^\top$, the velocity is $v_0 = [0.5 \ -0.9 \ 0]^\top$ and the reference point is $r = [1 \ 0 \ 0]^\top$. In $\text{SO}(3)$, the initial rotation matrix

is $X_0 = I_3$, the starting angular velocity matrix is $\Omega_0 = \begin{bmatrix} 0 & -0.5 & -1 \\ 0.5 & 0 & 0.7 \\ 1 & -0.7 & 0 \end{bmatrix}$ and

the reference inclination matrix was chosen as $R = \begin{bmatrix} -1 & 0 & 0 \\ 0 & 1 & 0 \\ 0 & 0 & -1 \end{bmatrix}$. Instead, the

Figure 7.2 illustrates a motion in a damped case. The parameters used in the simulation are the same as in the previous simulation, except that $\mu = 0.5$. The two oscillators are damped, therefore starting from their initial position and rotation (a) they will oscillate around the reference point and their reference inclination (d),

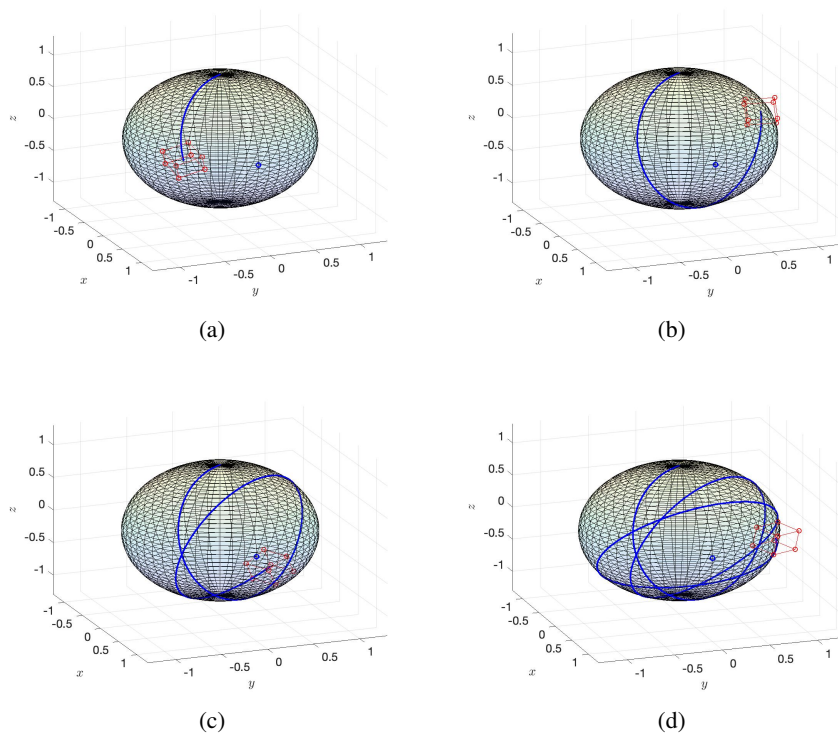


Figure 7.1: *Behaviour of the classic pendulum oscillator (4.4) on two different manifolds, in the absence of non-linear damping (namely, $\mu = 0$). Indicating by k the discrete-time stamp, the figure (a) shows the configuration of the system at $k = 2301$, the figure (b) at $k = 4461$, the figure (c) at $k = 9321$ and the figure (d) shows where the simulations stops, at $k = 1500$.*

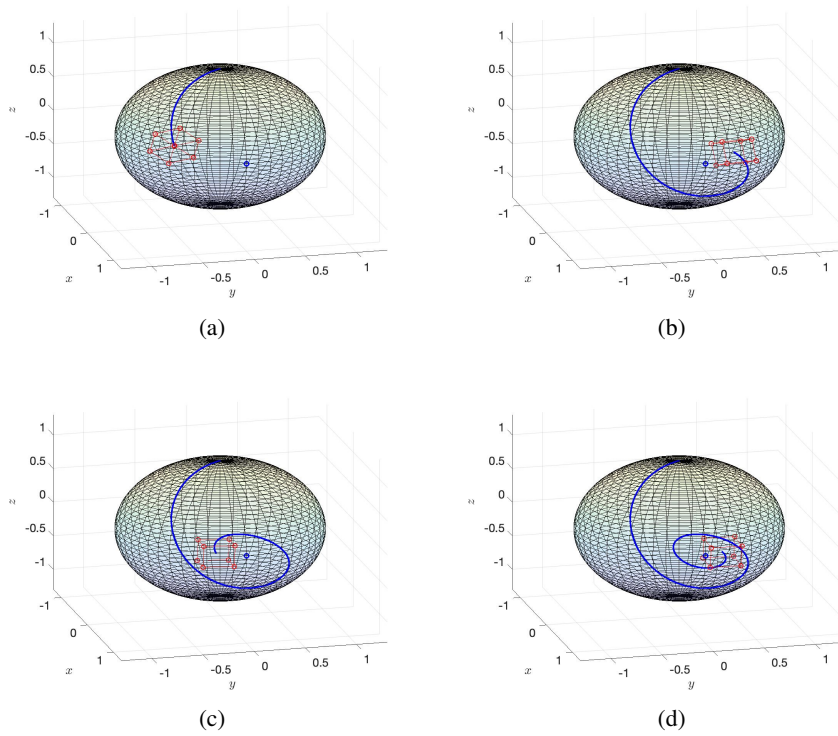


Figure 7.2: Behaviour of the classic pendulum oscillator (4.4) on two different manifolds, in the presence of non-linear damping. Indicating by k the discrete-time stamp, the figure (a) shows the configuration of the system at $k = 2,641$, the figure (b) at $k = 6,381$, the figure (c) at $k = 10,381$ and the figure (d) shows where the simulations stops, at $k = 15,000$.

until the references are reached.

8. Proportional-integral-derivative control theory

The proportional-integral-derivative control (PID) scheme is perhaps the most popular regulation theory [1]. The general idea to control a dynamical system into approaching a desired state trajectory is to compute an error signal and a control signal as a linear combination of the error signal itself (proportional control), of the time-derivative of the error signal (derivative control) and of an accumulated error signal (integral control).

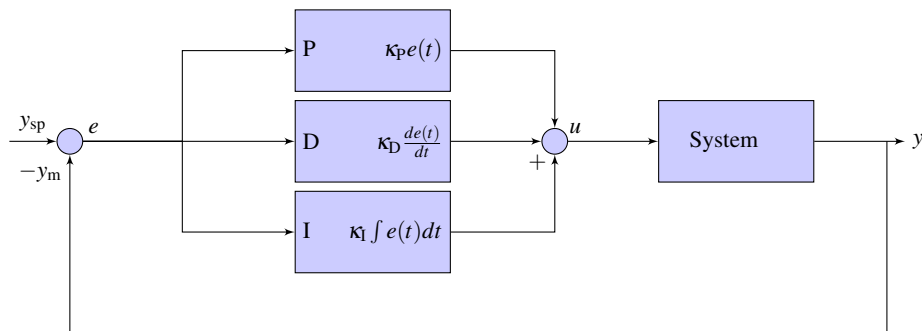


Figure 8.1: Classical PID control scheme, where y_{sp} denotes the set point, y_m denotes a measure of the controlled variable y , u denotes a control signal and e denotes an error signal, which quantifies the discrepancy between the measured controlled variable and the set point.

Increasing the proportional term coefficient κ_P makes the follower system be more "ready", which means using more energy, because the control effort would

be larger and it could also be useless to increase this term too much because it could cause a long series of overshoots with a consequent transient. The derivative term has the effect to stabilize the dynamics of the controlled system. The larger the coefficient κ_D , the lesser the oscillations around the set point. Finally, the integrative term is important to give to the controlled system some interesting and fundamental properties like error that tends to zero with respect to the set point and to reduce the impact of disturbances on the close loop system. Unfortunately, another effect of this term is to contrast the stabilization property of the derivative term, making the controlled system less stable and the convergence to the set point slower. The weight of its action is given by κ_I .

This section outlines possible extensions of a proportional-integral-derivative (PID) scheme to abstract systems whose state-spaces are smooth manifolds (i.e., state-manifolds).

A second-order system on a smooth manifold M is described by

$$\begin{cases} \dot{x}(t) = v(t), & t \geq 0, \\ \nabla_{\dot{x}(t)} v(t) = \mathbb{S}(t, x(t), v(t)) + u(t), \end{cases} \quad (8.1)$$

where $x(t) \in M$ denotes the system state, $v(t) \in T_{x(t)}M$ denotes the system velocity, $\mathbb{S} : \mathbb{R} \times TM \rightarrow TM$ denotes a time-varying state-transition map, and $u(t) \in TM$ denotes the system input vector field. The initial states are $x(0) = x_0 \in M$ and $v(0) = 0$. The system (8.1) may be rewritten compactly as

$$\nabla_{\dot{x}(t)} \dot{x}(t) = \mathbb{S}(t, x(t), \dot{x}(t)) + u(t), \quad t \geq 0, \quad (8.2)$$

which resembles a Newton's equation on the manifold M . (In fact, notice that, if the terms on the right-hand side are set to zero, the system evolves along a geodesically-uniform trajectory.) A second-order system admits *position control* as well as *velocity control*, which are discussed separately in the following.

8.1 Regulation of a second-order system by an M-PID controller

The purpose of a positional control is to drive the state $x(t)$ toward a reference point, which may be moving over time, denoted by $z(t) \in M$. The first step consists in defining an *error field*, which we take as

$$e(t) := \log_{x(t)} z(t) \in T_{x(t)}M, \quad (8.3)$$

that generalizes the Euclidean error $e(t) = z(t) - x(t)$ for the standard case that $M = \mathbb{R}^n$. Note that $e(t)$ is a tangent vector field in TM .

Note that, for a second-order system, it is often impossible to control the state-velocity directly as it is only possible to control the state-acceleration (as in a mass-spring-damper system, where the spring and the damper produce mechanical forces that affect the acceleration of the mass). A position M-PID controller may then be designed as:

$$u(t) := \kappa_P e(t) + \kappa_I \int_0^t \mathbf{P}^{x(\tau) \rightarrow x(t)}(e(\tau)) d\tau + \kappa_D \nabla_{\dot{x}(t)} e(t) + u_C(t) \in T_{x(t)} \mathbf{M}. \quad (8.4)$$

however, a choice like this would lead to a control strategy that is both computationally complicated to implement and theoretically inconclusive.

Therefore, on the basis of the previous discussion, we suggest the following control scheme that generalizes a PD scheme discussed in [9, 20]:

$$\begin{cases} \nabla_{\dot{x}(t)} \dot{x}(t) = \mathbb{S}(t, x(t), \dot{x}(t)) + u(t), & t \geq 0, \text{ (Second-order dynamical system)} \\ e(t) := \log_{x(t)} z(t), & \text{(Control error)} \\ \varepsilon(t) := \mathbf{P}^{z(t) \rightarrow x(t)}(\dot{z}(t)) - \dot{x}(t), & \text{(Control error velocity)} \\ \omega(t) := \int_0^t \mathbf{P}^{x(\tau) \rightarrow x(t)}(e(\tau)) d\tau, & \text{(Integrated control error)} \\ u(t) := \kappa_P e(t) + \kappa_I \omega(t) + \kappa_D \varepsilon(t) + u_C(t) & \text{(Control field)}. \end{cases} \quad (8.5)$$

with $u_C(t)$ to be defined. Taking the covariant derivative of the error field ε leads to:

$$\nabla_{\dot{x}} \varepsilon = \nabla_{\dot{x}} \mathbf{P}^{z \rightarrow x}(\dot{z}) - \mathbb{S}(t, x, \dot{x}) - u. \quad (8.6)$$

Plugging the equations (8.5) into the equation (8.6) yields

$$\nabla_{\dot{x}} \varepsilon = \nabla_{\dot{x}} \mathbf{P}^{z \rightarrow x}(\dot{z}) - \mathbb{S}(t, x, \dot{x}) - \kappa_P e - \kappa_I \omega - \kappa_D \varepsilon - u_C. \quad (8.7)$$

The term u_C is meant to cancel all terms in the tight-hand side of the above expression that do not depend on the error-type fields [19], namely:

$$u_C := \nabla_{\dot{x}} \mathbf{P}^{z \rightarrow x}(\dot{z}) - \mathbb{S}(t, x, \dot{x}). \quad (8.8)$$

The resulting error dynamics is governed by the equation

$$\nabla_{\dot{x}} \varepsilon + \kappa_P e + \kappa_I \omega + \kappa_D \varepsilon = 0. \quad (8.9)$$

The above second-order error system is characterized by the following result.

Theorem 8.1.1. *The error system (8.9) converges asymptotically to the state zero as long as $\kappa_P > 0$, $\kappa_D \geq 0$, $\kappa_I = \tilde{\kappa}_I \langle \omega, \varepsilon \rangle_x$, with $\tilde{\kappa}_I \geq 0$ (at least one among κ_D and $\tilde{\kappa}_I$ must differ from zero).*

Proof. The convergence of the synchronization error to zero is proven by showing that the following function is Lyapunov:

$$\mathcal{W}(x, z) := \frac{1}{2} \langle \varepsilon, \varepsilon \rangle_x + \frac{\kappa_P}{2} d^2(x, z). \quad (8.10)$$

The function \mathcal{W} is written as the sum of two terms, the first of which is always non-negative and, since the base-manifold M is Riemannian, the term $\langle \varepsilon, \varepsilon \rangle_x$ is zero only if $\varepsilon = 0$. The second term is non-negative because, by hypothesis, $\kappa_P > 0$. Deriving the function \mathcal{W} with respect to the time gives:

$$\begin{aligned} \dot{\mathcal{W}} &= \kappa_P \langle e, \varepsilon \rangle_x + \langle \nabla_{\dot{x}} \varepsilon, \varepsilon \rangle_x \\ &= \langle -\kappa_P e - \kappa_I \omega - \kappa_D \varepsilon, \varepsilon \rangle_x + \kappa_P \langle e, \varepsilon \rangle_x \\ &= -\kappa_D \langle \varepsilon, \varepsilon \rangle_x - \tilde{\kappa}_I \langle \omega, \varepsilon \rangle_x^2, \\ &\leq 0, \end{aligned} \quad (8.11)$$

which proves the assertion. □

Oddly enough, the value of the constant κ_P does not influence the rate of decrease $\dot{\mathcal{W}}$.

Notice that positional control implies velocity control (although the opposite is not true, in general).

8.2 Control efforts

The ‘control effort’ is a scalar index that quantifies the magnitude of the control field u . In physical control systems, the control effort is related to energy consumption of the actuator and its quantification is used to evaluate the suitability of an actuator with respect to a given control goal [14]. Formally, we define a control effort function $\sigma : TM \rightarrow \mathbb{R}$ as:

$$\sigma := \frac{1}{2} \|u\|_x^2. \quad (8.12)$$

Likewise, we define a control effort function $\sigma_C : TM \rightarrow \mathbb{R}$ and a function $\sigma_{PID} : TM \rightarrow \mathbb{R}$ associated to the ‘cancelling’ component of the control field and to the PID component of the same control field, as:

$$\sigma_C := \frac{1}{2} \|u_C\|_x^2, \quad \sigma_{PID} := \frac{1}{2} \|u - u_C\|_x^2. \quad (8.13)$$

It is important to evaluate the control efforts associated to the different components of the above-proposed M-PID control schemes. It is clear that the control effort σ_{PID} is directly related to the parameters κ_P , κ_I , κ_D .

8.3 Application of the general M-PID control theory to time-synchronization of second-order systems

Synchronization of systems on manifolds is an instance of non-linear control where the reference trajectory is generated by a dynamical system (which may coincide with, or differ from, the controlled system). The dynamical system that provides a reference is termed *leader*, described by a state-transition operator \mathbb{S}_L , while the controlled system will be referred to as *follower*, described by a state-transition operator \mathbb{S}_F . We suggest the following leader-follower synchronization scheme:

$$\left\{ \begin{array}{l} \dot{z}(t) = w(t), \nabla_{w(t)} w(t) = \mathbb{S}_L(t, z(t), w(t)), t \geq 0, \text{ (Leader dynamical system)} \\ \dot{x}(t) = v(t), \nabla_{v(t)} v(t) = \mathbb{S}_F(t, x(t), v(t)) + u(t), \text{ (Follower dynamical system)} \\ e(t) := \log_{x(t)} z(t), \text{ (Control error)} \\ \varepsilon(t) := \mathbf{P}^{z(t) \rightarrow x(t)}(\dot{z}(t)) - \dot{x}(t), \text{ (Control error velocity)} \\ \omega(t) := \int_0^t \mathbf{P}^{x(\tau) \rightarrow x(t)}(e(\tau)) d\tau, \text{ (Integrated control error)} \\ u_C(t) := \nabla_{\dot{x}(t)} \mathbf{P}^{r(t) \rightarrow x(t)}(\dot{z}(t)) - \mathbb{S}_F(t, x(t), \dot{x}(t)), \text{ (Cancelling component)} \\ u(t) := \kappa_P e(t) + \kappa_I \omega(t) + \kappa_D \varepsilon(t) + u_C(t), \text{ (M-PID control field)} \end{array} \right. \quad (8.14)$$

The term u_C apparently ‘cancels’ the internal dynamics of the follower system and replaces it with a copy of the internal dynamics of the leader system. Notice that the leader system dynamics and the follower system dynamics have been split in two first-order equations by introducing two velocity fields v, w .

In order to implement the leader system, the controlled follower system and the control scheme on a computing platform, it is necessary to come up with discrete-time versions of the equations (8.14).

The first step consists in replacing the continuous-time variable t with a discrete-time index $k = 0, 1, 2, \dots$ related by $t = hk$, where $h > 0$ is a discretization stepsize that is generally much smaller than 1. Likewise, the continuous-time variables describing the dynamics of the systems as well as the control field will be replaced by their discrete-time counterparts.

The equations (8.14) are then replaced by their numerically-approximated counterparts and, in particular, the approximation (2.3) was repeatedly made use

of:

$$\begin{cases}
 z_{k+1} := \exp_{z_k}(h w_k), \quad k = 0, 1, 2, \dots, \\
 w_{k+1} := \mathbf{P}^{z_k \rightarrow z_{k+1}}(w_k + h \mathbb{S}_L(hk, z_k, w_k)), \\
 x_{k+1} := \exp_{x_k}(h v_k), \\
 v_{k+1} := \mathbf{P}^{x_k \rightarrow x_{k+1}}(v_k + h \mathbb{S}_F(hk, x_k, v_k) + h u_k), \\
 e_k := \log_{x_k} z_k, \\
 \varepsilon_k := \mathbf{P}^{z_k \rightarrow x_k}(w_k) - v_k, \\
 \omega_k := \begin{cases} h e_0, & \text{if } k = 0, \\ \mathbf{P}^{x_{k-1} \rightarrow x_k}(\omega_{k-1}) + h e_k, & \text{if } k > 0, \end{cases} \\
 u_{C,k} := \begin{cases} -\mathbb{S}_F(0, x_0, v_0), & \text{if } k = 0, \\ \frac{1}{h} (\mathbf{P}^{r_k \rightarrow x_k}(w_k) - \mathbf{P}^{x_{k-1} \rightarrow x_k}[\mathbf{P}^{r_{k-1} \rightarrow x_{k-1}}(w_{k-1})]) - \mathbb{S}_F(hk, x_k, v_k), & \text{if } k > 0, \end{cases} \\
 u_k := \kappa_P e_k + \kappa_I \omega_k + \kappa_D \varepsilon_k + u_{C,k},
 \end{cases} \tag{8.15}$$

where $x_0, z_0 \in \mathbf{M}$, $v_0 \in T_{x_0} \mathbf{M}$ and $w_0 \in T_{z_0} \mathbf{M}$ are given initial states. The dynamics of the leader system is described by the variables pair $(z_k, w_k) \in T\mathbf{M}$ and the dynamics of the follower is described by the variables pair $(x_k, v_k) \in T\mathbf{M}$. The flow of the continuous-time dynamics of the systems has been approximated numerically by a forward Euler stepping [8], while special care has been devoted to the numerical approximation of the cumulative error control term ω_k (via an transported-accretion method) and of the cancelling component of the control field $u_{C,k}$ (via an incremental-ratio-type approximation of covariant derivation).

It is worth noticing that, in the equation to compute the cancelling component of the control field, in general $\mathbf{P}^{x_{k-1} \rightarrow x_k} \circ \mathbf{P}^{r_{k-1} \rightarrow x_{k-1}} \neq \mathbf{P}^{r_{k-1} \rightarrow x_k}$. The equality holds only when the three points belong to the same geodesic arc. however, upon synchronization, r_k and x_k are pretty close to one another and so are x_k and x_{k-1} because of the small value of the stepsize h , therefore, from a numerical point of view, the equation to compute the cancelling component of the control field might be replaced by:

$$u_{C,k} := \frac{1}{h} (\mathbf{P}^{r_k \rightarrow x_k}(w_k) - \mathbf{P}^{r_{k-1} \rightarrow x_k}(w_{k-1})) - \mathbb{S}_F(hk, x_k, v_k), \quad k > 0. \tag{8.16}$$

The above numerical approximation is lighter in computational complexity than the approximation in (8.15).

A better numerical approximation of the actual flows of the system might be obtained by replacing the forward Euler stepping method with higher-order numerical stepping schemes, such as second-order Heun and Runge schemes and a fourth-order Runge-Kutta scheme [8]. In the present context, a forward Euler

scheme looks adequate to illustrate the behavior of the control scheme devised in the above sections.

9. Numerical simulations and experiments

In this section, synchronization of second-order oscillators by the M-PID control theory will be illustrated through a number of numerical simulations aimed at investigating several interesting aspects, such as speed of synchronization, magnitude of the control efforts, and effectiveness in synchronizing two ‘twin’ systems as well as a leader and a follower that differ structurally to one another. In the present document there are the results of several simulations of the synchronization process of two oscillator with the same dynamics (considering in particular hard Duffing oscillators) or even with different dynamics, namely, two different oscillators (considering in particular the case of a soft Duffing and a hard duffing oscillator). Another studied variation to the problem is the case in which the two oscillators have two different reference points (plotted on the sphere using different colors).

The initial conditions (initial position and initial velocity) of the two systems are taken randomly and so they could be more or less favorable to reach a fast synchronization. The graphics of kinetic, potential and total energy are plotted on the same graphic window with the distance between the states of the two systems on the sphere, the distance of each system from its reference point and a scalar quantification of the control effort over time. A sufficient and necessary condition to the reaching of synchronization between the two systems is that the distance $d(z, x)$ tends to zero, because the two systems have to follow the same trajectory at the end of the simulation (assuming that the duration of the simulation is long enough).

Instead, the fact that the graphic of the distances between each oscillator trajectory and its own reference point follow the same trajectory after a certain value of time is not a necessary and sufficient condition of synchronization, because it depends on whether the two reference points are the same or not. In fact, if they

are different, for each system the graphic of distance from the own reference point would oscillate independently, because the follower and the leader achieve synchronization, so the same trajectory, but the distances from the reference points are different because they are two distinct points. The same considerations apply to potential energies that oscillate independently, being the reference points different.

Synchronization is achieved asymptotically, after an initial transient when the difference between the two trajectories is larger. It is also interesting to notice that the total energy of the follower system will not result to be constant over time and this is easily explicable: the follower is not an isolated system which does not interact with the external environment. In fact it is subject to the M-PID control which is another independent system with an own power supply used to correct the follower's trajectory in order to adapt to the leader's one. So, initially, the follower system will have a surplus of energy, and over time it will reach a constant value, because, once achieved synchronization, the control effort progressively reduces, tending to zero at regime. Instead, the leader is an isolated system ideally and so it is not subject to external forces that change its total energy which keeps constant over time. Talking about the control effort, at the beginning it has high values, and it tends to zero over time, upon reaching synchronization. In particular looking at the kinetic energies of the follower and the leader, it can be noticed that they reach synchronization, that confirms that the synchronization of position implies the synchronization of velocity (because kinetic energy depends only from one variable that is velocity). Instead talking about synchronization, it can be considered that the error system (8.6) is linear, so it is possible to extend some considerations from classical control theory on flat spaces to the case of manifolds studied in this document. The control field (8.4) is calculated on the basis of an error term, of its derivative and of its integral with respect to time (without considering the added term u_C to delete the internal dynamics of a system), so it will be composed by a proportional term, a derivative term and an integral term.

How is synchronization reached changing the values of these terms (so changing the value of the corresponding coefficients) ? The results obtained are similar to the known case in a flat space. Increasing the proportional term coefficient, the follower system will be more "ready" and will adapt to the leader system in a short time, which, however, means using more energy, because the control effort would be greater and it could also be useless to increase this term too much because it could cause a long series of overshoots with a consequent slow transient to the desired synchronization. The derivative term has the effect to stabilize the trajectory of the follower controlled by M-PID. It decreases the oscillations around the desired set point, getting a stable dynamics that does not oscillate too much. Finally, the integral term is important to endow a controlled system with some interesting and fundamental properties like an error field with respect to the reference

state that tends to zero and to reduce the impact of disturbances on the closed-loop system. Unfortunately, another effect of this term is to contrast the stabilization property of the derivative term, making the controlled system less stable and the synchronization slower. All these known properties of classical PID controllers can be extended to the case of control of systems whose state belongs to a smooth manifold.

M-PID tuning corresponds to the choice of the best weights to give to proportional, derivative and integral terms in order to get a controlled system that is performing better (and that achieves a faster synchronization, in this particular case). As discussed, the effects of the three terms are multiple and conflicting therefore, to get the best M-PID tuning, it would be necessary to adopt an optimal control strategy [23], which will not be treated in the present document.

In most of the following numerical simulations, the leader's dynamics starting point was set to $z_0 = [0 \ 1 \ 0]^\top$ and its initial velocity was set to $w_0 = [1 \ 0 \ 0.8]^\top$, while the follower's starting point was taken as $x_0 = [0 \ 0 \ 1]^\top$ and its initial velocity was taken as $v_0 = [-1.5 \ -1.5 \ 0]^\top$. The reference points for the leader and the follower oscillators are $r_L = r_F = [0 \ 0 \ -1]^\top$.

9.1 Evaluation of the action of the cancelling component of the control field

The control field (8.4) can be split into two contributions:

- u_C that deletes the internal dynamics of the follower;
- $u - u_C$ that provides the synchronization.

The two contributions can be represented graphically over time by means the total control effort, which is the sum of them, as well as by partial control efforts, as defined in (8.12) and (8.13). Several simulations carried out lead to the conclusion that the contribution of the term u_C in the M-PID is not indispensable for reaching the synchronization of the oscillators. In fact, u_C is a control term whose purpose is to cancel the internal dynamics of the follower, which anyway would be modified by the control action provided by M-PID control even without the u_C term. Nevertheless, the term u_C gives an improvement in the reaching of synchronization. In particular, we observed an improvement in the “readiness” of the follower system, which will adapt to the leader system faster. In fact, especially in the case (showed in several simulations) where the initial velocity of the follower system is completely opposite to the velocity imposed from the leader system and it is also

of large intensity, taking out the u_C term the M-PID controller would take longer time to modify the trajectory of the follower system. This behavior appears obvious because the M-PID controller imposes a force on the follower system (that possesses its own inertia) to make it follow the leader, but it is readily understood how it is easier to control the a “dead body” without any intrinsic dynamics than a body moving in the space according to its own dynamics. On the other hand, there is the case in which the follower systems initial velocity is in the right direction (according to the leader trajectory), so the u_C term would be useless (because, in this case, the intrinsic dynamics of the follower would take it around the leader and so deleting its dynamics would be a waste of energy), while using only the simple control field provided by the M-PID the follower trajectory would be only modified to synchronize to the leader. Instead with the u_C term, that deletes the internal dynamics of the follower system, the latter will immediately start to follow the leader trajectory independently from its own initial conditions. These considerations are more evident in the case of different dynamical systems, where the two systems to synchronize have not only different initial conditions, but also different internal dynamics.

A numerical experiment implemented in the present document consists in controlling initially the follower with both the components of the control field and, at a pre-fixed time, in switching off the u_C term. The observed behavior is different if the two oscillators possess the same structure and when they differ from one another. In the following, we present the results of two simulations in which u_C is turned to zero from half of the time-range considered. The two simulations are illustrated in the Figure 9.1. Infact it can be noticed that in the case with the same oscillators, looking at the distance graphics, there are no differences from the previous cases. While if the two oscillators are different, for example a hard duffing oscillator and a soft Duffing one, the graphic of the distance rapidly changes when u_C is reduced to zero. The instant when u_C is turned to zero corresponds to the increase of the remaining contribution of the M-PID. It seems to react instantly, but zooming in the graphic, the real dynamics presents an initial and short transient before reaching the regime value. Plotting separately the two contributions of control effort it can be seen that u_C contribution is larger than the remaining part of the control field u (namely, $u - u_C$).

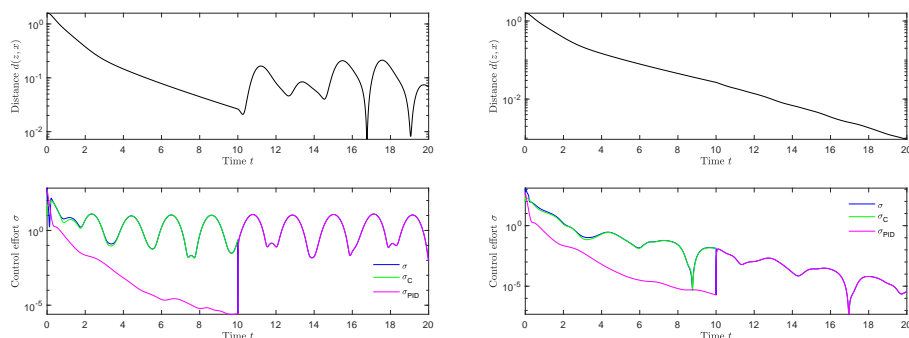


Figure 9.1: Synchronization of two Duffing-type oscillators by a M-PID controller. The left-hand panel shows the values of the distance $d(z, x)$ on the top and of the control effort σ on the bottom, taken by a hard Duffing oscillator and a soft Duffing oscillator. Instead, the right-hand panel shows the values of the distance $d(z, x)$ on the top and of the control effort σ on the bottom, taken by two hard Duffing oscillators. In both cases, the follower is controlled by an M-PID controller with u_C in the first 10 seconds of the simulation and from $t = 10$ it is set to zero. The proportional control coefficient was set to $\kappa_P = 10$, the integral control coefficient was set to $\kappa_I = 5$ and the derivative control coefficient was set to $\kappa_D = 10$.

9.2 Evaluation of the action of M-PID controllers on twin oscillators with identical reference points

The following considerations will deal with the case of two oscillators with the same reference point, in order to make synchronization more evident.

Synchronization of two hard Duffing oscillators on the sphere \mathbb{S}^2 has been simulated. If there is only the proportional term, the two oscillators do not achieve synchronization, as shown in the Figure 9.2, because the information about the error's dynamics is not sufficient for calculating an effective control field. This result is coherent with the theoretical findings summarized in the Theorem 8.1.1, according to which, a second-order system needs at least a derivative or an integral term, besides the proportional term, to be effective.

At the same time, the proportional term is essential for synchronization because it is the term that provides the largest contribution in term of energy to the control field in order to reach the leader's trajectory. It can be noticed from the results shown in the Figure 9.3 that in the simulations with both integral and derivative terms the distance between the states of the two oscillators over time tends to zero more quickly and regularly, without ripples. Instead, if the control field is composed only by the proportional term and the integral term, synchronization is

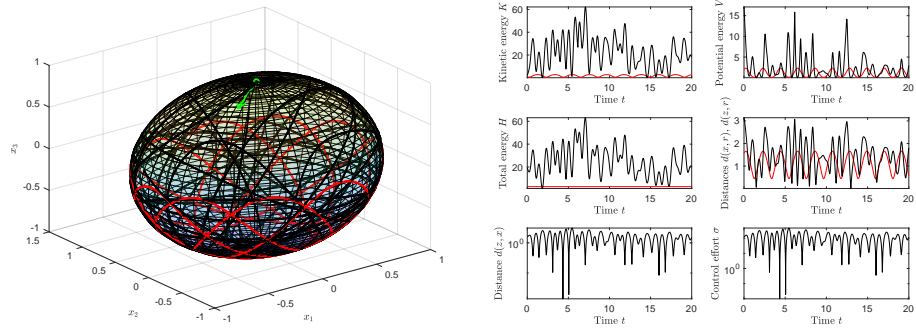


Figure 9.2: Synchronization of two hard Duffing oscillators where the follower is controlled by a P-controller (a M-PID with only the proportional term). In both panels the black lines are about the follower dynamics while the red lines are referred to the leader dynamics. The left-hand panel shows the trajectories on the sphere. The follower's initial velocity is represented by the green arrow. The right-hand panel shows the values taken by the kinetic energy, the potential energy, the total energy and the control efforts and distances over the generated trajectory. The proportional control coefficient was set to $\kappa_P = 0.01$.

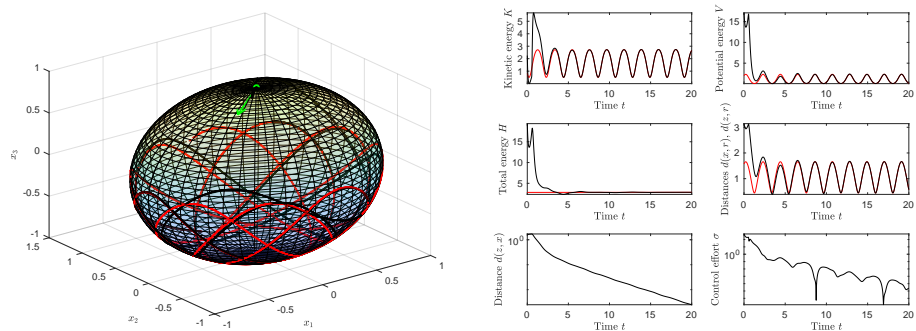


Figure 9.3: Synchronization of two hard Duffing oscillators where the follower is controlled by a full M-PID controller. Values and graphic elements are as in the Figure 9.2. The integral control coefficient is $\kappa_I = 5$, the derivative control coefficient is $\kappa_D = 10$ and the proportional control one is $\kappa_P = 10$.

slower and the distance function tends to zero slowly, as illustrated numerically in the Figure 9.4. If there are only the proportional and derivative terms, the initial

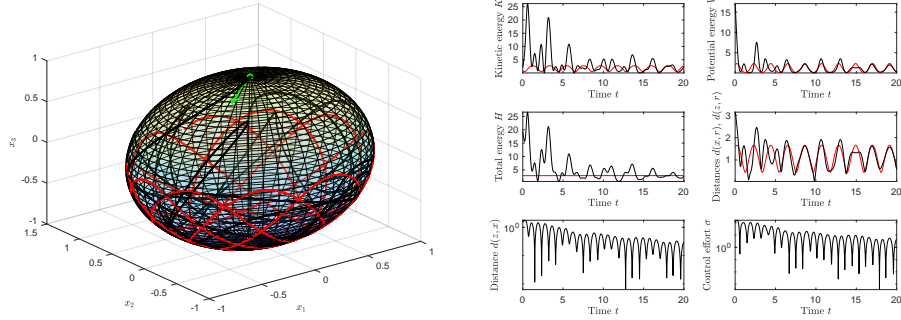


Figure 9.4: *Synchronization of two hard Duffing oscillators where the follower is controlled by a PI-controller, with only the proportional and integral terms. Values and graphic elements are as in the Figure 9.2. The integral coefficient was set to $\kappa_I = 2.5$ and the proportional term coefficient was set to $\kappa_P = 10$.*

transient is shorter compared to the case with all contributions, because the integral term decreases the system's stability, as it can be readily observed from the results displayed in the Figure 9.5. The same consideration can be made in the case of two

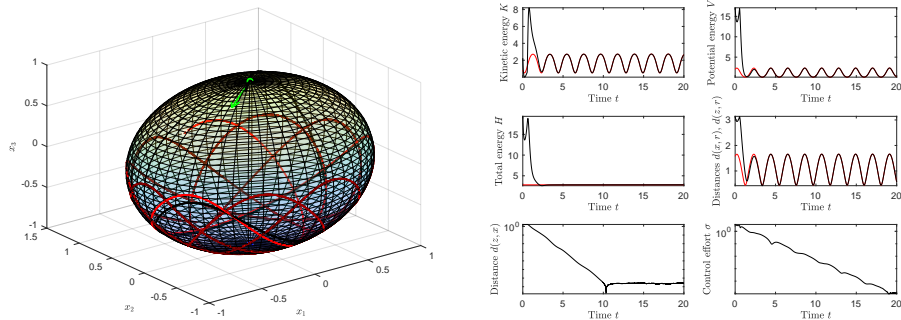


Figure 9.5: *Synchronization of two hard Duffing oscillators where the follower is controlled by a PD-controller, with only the proportional and derivative terms. Values and graphic elements are as in the Figure 9.2. The derivative control coefficient is $\kappa_D = 10$ and the proportional control coefficient is $\kappa_P = 10$.*

oscillators with the same dynamics, for example two hard Duffing oscillators, but with two different reference points.

The theory studied for PID applied to systems on a flat space, from simulations,

seem to be valid also for the case of a system on manifold. For example, it is known that the proportional term moves the trajectory of the system controlled near the reference trajectory (in this case the leader's one), but the system will show overshoots for values of this term too large. This is valid (in a limited range of variation of κ_P) also in the case of oscillators on manifold as it can be seen in the simulations illustrated in the Figure 9.6, where it has been changed only the value of κ_P coefficient and the other (integral and derivative coefficients) are kept constant. As it can be noticed, before synchronization is reached there is an initial

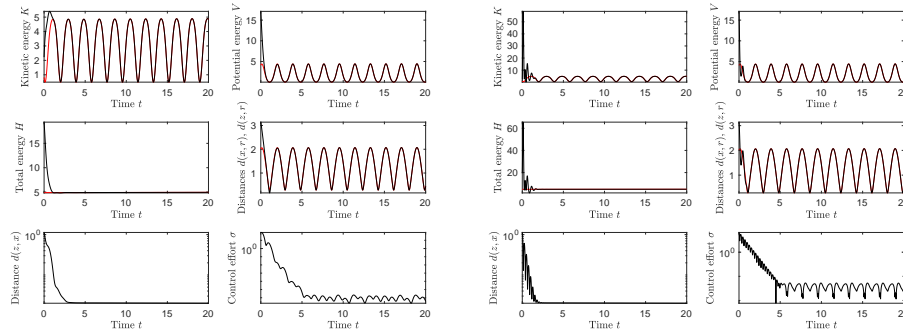


Figure 9.6: Synchronization of two hard Duffing oscillators where the follower is controlled by PID controller: comparison with two different values of proportional term coefficient. In both panels, the black lines denote the follower's dynamic, while the red lines denote the leader's dynamic. The left-hand panel shows the values taken by the kinetic energy, the potential energy, the total energy, control effort and distances over the generated trajectory, when the proportional coefficient $\kappa_P = 5$. The right-hand panel shows the same quantities when the proportional coefficient $\kappa_P = 150$. In both cases, integral coefficient is $\kappa_I = 5$ and derivative coefficient is $\kappa_D = 5$.

transient with overshoots of the follower oscillator near the leader's trajectory.

Instead, the derivative term of the PID control scheme has the property to stabilize the trajectory of the controlled system, decreasing oscillations (in fact, in the continuous-time case, the derivative term corresponds to a zero of the transfer function in the origin of the Laplace space, that stabilizes the system and shortens the transient). It can be verified from the two following simulations that this is valid also in the case studied here (for limited variation range of κ_I). In the results displayed in the Figure 9.7, the coefficients κ_D and κ_P have the same value while κ_D changed. If the derivative coefficient is larger, the follower trajectory is stabilized on the leader one, while if the derivative coefficient is lower, it is characterized by ample oscillations around leader trajectory before stabilizing.

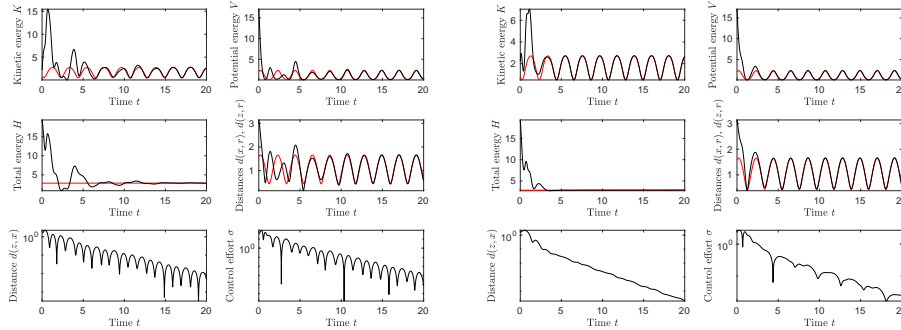


Figure 9.7: Synchronization of two hard Duffing oscillators where the follower is controlled by PID controller: comparison with two different values of derivative term coefficient. Values and graphic elements are as in the Figure 9.6. The left-hand panel shows results when the derivative coefficient is $\kappa_D = 0.5$, while the right-hand panel shows results when the derivative coefficient is $\kappa_D = 3$. In both cases, the integral coefficient is $\kappa_I = 25$ and the proportional coefficient is $\kappa_P = 5$.

Finally, the integral term has the property to reduce the permanent regime error and the unwanted effect of disturbances (in fact in the continuous-time case, the integral term corresponds to a pole of the transfer function at the origin in the Laplace space, that introduces an internal model for step inputs (disturbances or reference functions)). From the following two simulations it can be seen that this is valid also for the studied case, in a limited range of variation for κ_I . Similarly to the previous simulations, κ_D and κ_P have been maintained constant, while only κ_I has been changed. The results are displayed in the Figure 9.8. In the case with a lower value of the integrative coefficient the distance between the follower and the leader trajectories tends to zero slower, while if its value is larger the distance function tends to zero more quickly. At the same time, it is known that the integral term decrease the stabilizing effect of derivative term, in fact it can be seen that if the integrative coefficient is larger the follower trajectory has oscillations around leader one, while if it is lower this negative effect is negligible.

These considerations can be extended to the case with a control effort composed not only by proportional, derivative and integrative terms, but also by u_C whose aim is to delete the internal dynamics of the follower system. In fact, as already said, the presence of u_C can make synchronization quicker if the own dynamics of the follower tends to take the system far from the leader, but the PID contribution is the same: the contribution u_C changes the duration of the transient. The results are also the same if the two oscillators considered are different in their reference points, but also in their dynamics (in particular, a hard Duffing and a soft

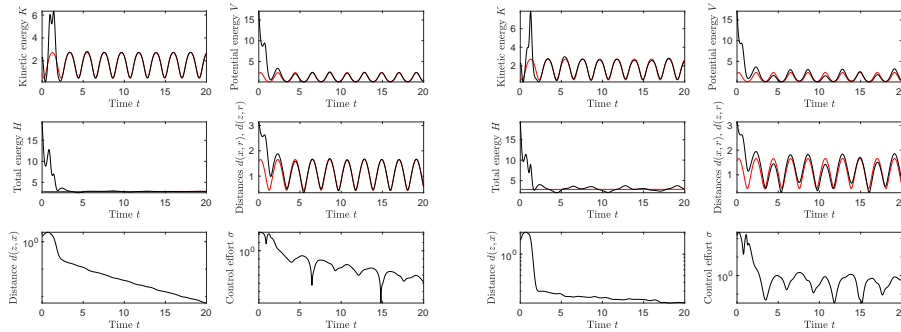


Figure 9.8: Synchronization of two hard Duffing oscillators where the follower is controlled by PID controller: comparison with two different values of integral term coefficient. Values and graphic elements are as in the Figure 9.6. The left-hand panel shows results when the integral coefficient is $\kappa_I = 3$, while the right-hand panel shows results when the value of the integral coefficient is $\kappa_I = 25$. In both cases, the derivative coefficient is $\kappa_D = 5$ and the proportional coefficient is $\kappa_P = 5$.

Duffing oscillator have been considered).

The Figures 9.9 and 9.10 show a comparison between the case with u_C and without u_C , respectively, with the follower initial velocity (represented in the figure on the sphere as a tangent vector) with a direction unfavorable for the convergence to the leader trajectory (because it is opposed to it). It can be noticed from the Figures 9.9 and 9.10 that the presence of the u_C term makes synchronization quicker because the internal dynamics of the follower oscillator would take it far from the leader trajectory. In fact, in the case with u_C the initial transient is shorter than without u_C .

The Figures 9.11 and 9.12 illustrate a comparison between the case with u_C and without u_C , respectively, with the follower initial velocity (represented in the figure on the sphere as a tangent vector) with a direction favorable for the convergence to the leader trajectory (because it is directed towards it). Moreover from the Figures 9.11 and 9.12, it can be seen that the initial transient is shorter in the case without u_C because, in this case, it is not useful to delete the follower internal dynamics, in fact, this component of the control field tends to take the follower oscillator near the leader trajectory. It would be a useless waste of energy of the PID controller. Therefore, the choice of a M-PID controller with the u_C term or without it is a problem that has not an univocal solution, but it depends on the case considered.

The simulations shown in the Figure 9.13 illustrate the case of two hard Duffing oscillators with two different reference points. Although synchronization is reached, the potential functions oscillates in phase over time but with different tra-

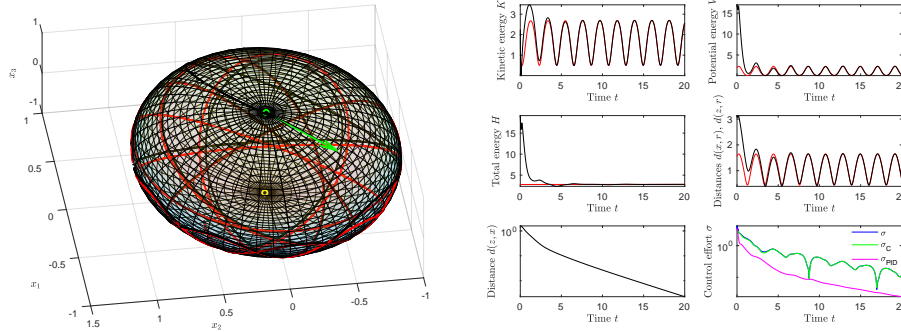


Figure 9.9: Synchronization of two hard Duffing oscillators where the follower is controlled by a M-PID controller with u_C term and the initial velocity direction of the follower is not favorable for synchronization (i.e., it is opposed to the leader trajectory). In both panels the black lines indicate the follower's dynamics, while the red lines indicate the leader's dynamics. The left-hand panel shows the trajectories of the two oscillators on the sphere over time. The follower's initial velocity is represented by a green arrow and his starting point with a green point, instead the leader's starting point is represented by a white point. The right-hand panel shows the values taken by the kinetic energy, the potential energy, the total energy and control effort and distances over the generated trajectory. In particular, in the panel at the right-bottom corner, the total control effort σ is represented in blue, the PID contribution σ_{PID} in magenta and the contribution deriving from u_C in green color. The proportional control coefficient is $\kappa_P = 10$, the integral control coefficient is $\kappa_I = 5$ and the derivative control coefficient is $\kappa_D = 10$.

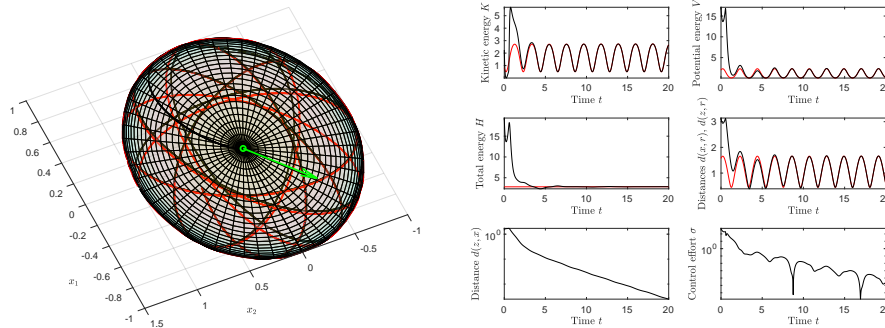


Figure 9.10: Synchronization of two hard Duffing oscillators where the follower is controlled by a M-PID controller without the u_C term and the initial velocity direction of the follower is not favorable for synchronization. Values and graphic elements are as in the Figure 9.9.

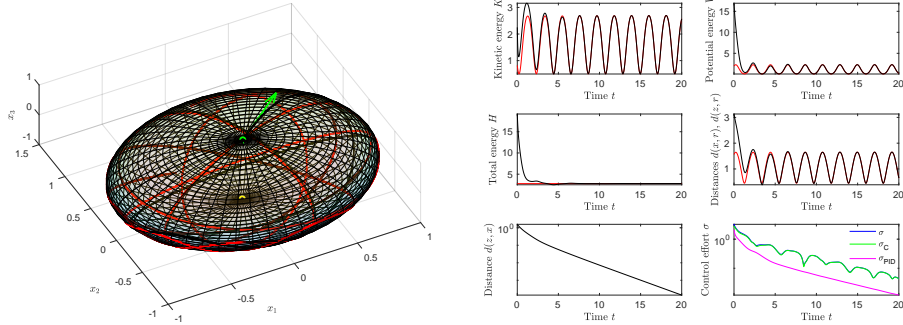


Figure 9.11: Synchronization of two hard Duffing oscillators where the follower is controlled by a M-PID controller with the u_C term when the initial velocity direction of the follower is favorable for synchronization. In both panels the black lines denote the follower's dynamics, while the red lines denote for the leader's dynamics. The left-hand panel shows the trajectories of the two oscillators on the sphere over time. The follower's initial velocity is represented by a green arrow and his starting point with a green point, instead the leader's starting point is represented by a white point. The right-hand panel shows the values taken by the kinetic energy, the potential energy, the total energy and control effort and distances over the generated trajectory. In particular, the right-bottom panel shows the total control effort σ in blue, the PID contribution σ_{PID} in magenta and the contribution deriving from u_C in green color. The proportional control coefficient is $\kappa_P = 10$, the integral control coefficient is $\kappa_I = 5$ and the derivative control coefficient is $\kappa_D = 10$.

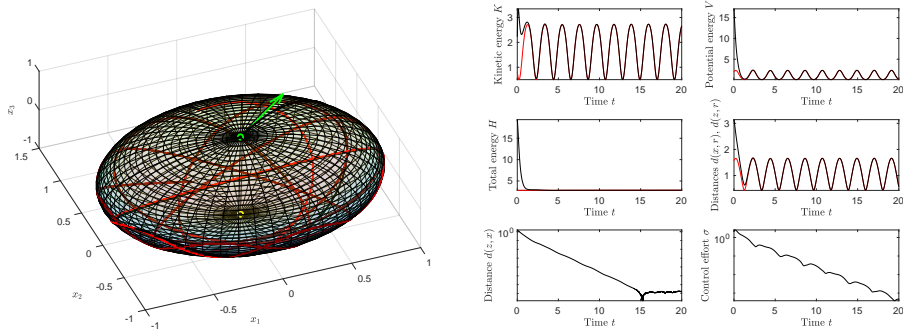


Figure 9.12: Synchronization of two hard Duffing oscillators where the follower is controlled by a M-PID controller without the u_C term when the initial velocity direction of the follower is favorable for synchronization. Values and graphic elements are as in the Figure 9.11.

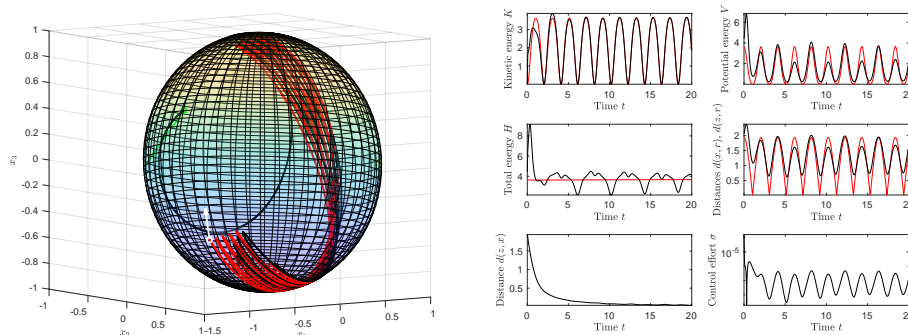


Figure 9.13: Synchronization of two hard Duffing oscillators where the follower is controlled by M-PID controller. Moreover in both panels the black lines denote the follower's dynamics, while the red lines denote the leader's dynamics. The left-hand panel shows the trajectories of the two oscillators on the sphere over time. The follower's initial velocity is represented by green arrow, while the leader's initial velocity is represented by a white arrow. The two different reference points have been represented as two colored points on the sphere (green for the leader reference point and white for the follower's one). The right-hand panel shows the values taken by the kinetic energy, the potential energy, the total energy and control effort and distances over the generated trajectory. In this case, the leader's and follower's starting points, initial velocities and reference points are taken randomly. Moreover the proportional control coefficient is $\kappa_P = 10$, the coefficient of the integral control term is $\kappa_I = 5$ and the derivative coefficient is $\kappa_D = 10$.

jectories: this is due to the fact that the follower and the leader, after synchronization, follow the same trajectory, but, being the reference points two different points on the sphere, the distances (as it can be noticed from the curve of the distances $d(x, r)$ and $d(z, r)$) will be different like the potential functions. Another interesting observation is that the total energy of the follower will not tend to a constant value but continues to change over time: this is due to the control field which has to act continuously over time, because of the follower reference point's force that tends to move away the follower from the leader trajectory. Instead, in the case with the same reference points the total energy tends to a constant value, because, after an initial transient, the control effort is very low.

Finally, in the simulations shown in the Figure 9.14 and 9.15, it is illustrated a case-study with two oscillators possessing different dynamics, in particular, the synchronization of a hard Duffing and a soft Duffing oscillator is taken into consideration. The Figure 9.14 shows the synchronization behavior of a M-PID controller endowed with the u_C term, while the results illustrated in Figure 9.15 were obtained without this term, but there are only the proportional, derivative and integrative terms. It can be noticed that the u_C term makes synchronization quicker, in fact the distance function tends quickly to zero. As already mentioned, by changing the values of the PID parameters (proportional, derivative and integrative coefficients) it can be noticed that all the properties studied for the linear systems' control are valid also for the oscillators that are non-linear systems (in particular they are systems of the second order because in their dynamics there are two differential equations, one for velocity and one for the position).

These simulations, concerning control by M-PID to achieve the synchronization of two oscillators with the same or different dynamics, is a sort of "toy problem" before the study of synchronization of two real-world rigid bodies in the space, like two gyrostat satellites and quadcopter drones, with their inertia.

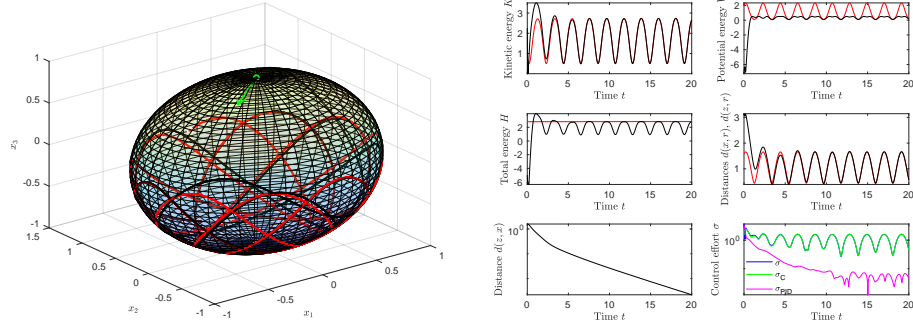


Figure 9.14: Synchronization of an hard Duffing oscillator and a soft Duffing oscillator, where the follower is controlled by a M-PID controller with the presence of the u_C term. In both panels the black lines stand for the follower's dynamic, while the red ones stand for the leader's dynamic. The left-hand panel shows the trajectories of the two oscillators on the sphere over time. The follower's initial velocity is represented by the green vector in the figure. The right-hand panel shows the values taken by the kinetic energy, the potential energy, the total energy and control effort and distances over the generated trajectory. In particular in the right-bottom panel, the total control effort σ is represented in blue, the PID contribution σ_{PID} in magenta and the contribution deriving from u_C in green color. The proportional control coefficient is $\kappa_P = 10$, the integral control coefficient is $\kappa_I = 5$ and the derivative control coefficient is $\kappa_D = 10$.

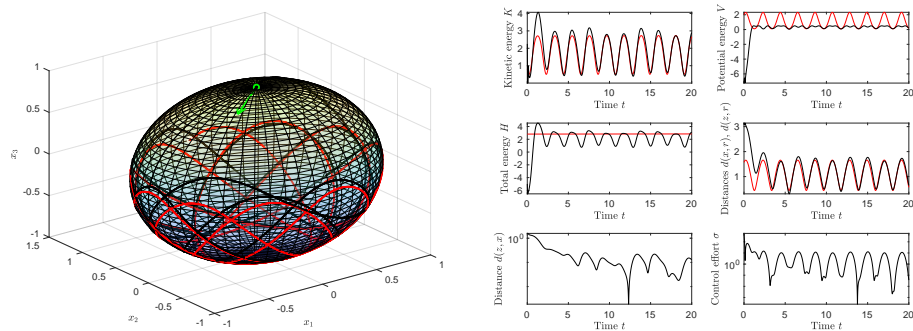


Figure 9.15: Synchronization of an hard Duffing oscillator and a soft Duffing oscillator, where the follower is controlled by a M-PID controller without the u_C term. Values and graphic elements are as in the Figure 9.14.

10. Conclusion

The present document outlined the mathematical structure of a general second-order dynamical system on manifolds and on Lie groups expressed through the language of manifold calculus and Lie-group theory. The studied dynamical systems are governed by a smooth vector field that describes the infinitesimal motion of a point under its flow. Compared to the familiar case where $M = \mathbb{R}^n$, the manifold setting requires more conceptual work to properly define what is meant by the vector field at a point. In the latter case, the dynamics takes place in the tangent bundle, but when $M = \mathbb{R}^n$ the tangent plane at a point is isomorphic to the manifold itself. A number of instances of the general dynamical systems were presented and discussed, leading to defining a number of abstract non-linear oscillators on manifolds and Lie groups. A large portion of this document was devoted to developing numerical methods to implement these systems on a computing platform and in testing these methods through numerical simulations. Most simulations were carried out by means of an extension of the forward Euler method, although more accurate, second-order methods, such as the Heun scheme and the Runge (RK2) scheme were also presented and utilized to illustrate the benefits of higher-order numerical integration schemes.

Moreover in the second part of the manuscript, it has been discussed the problem of synchronization of two second-order, time-varying dynamical systems whose state space is not a flat field but rather a curved Riemannian manifold. This problem involves a leader system, which evolves independently, and a follower system, which is bound to synchronize over time to the leader. Synchronization is achieved by means of a control law that generates a control field that drives the follower. The control law is an extension of the classical proportional-integral-derivative control scheme to curved manifolds.

Even the theoretical content of this second part of the paper has been complemented by several numerical experiments which illustrated its properties and features. We point out that the contribution u_C of the M-PID control scheme is not fundamental for reaching the synchronization of two oscillators. However, it

entails a huge improvement to get faster synchronization. This advantage can be noticed even more when there are different oscillators with different internal dynamics.

The numerical results revealed the richness and beauty of the developed non-linear oscillator theory on smooth manifolds.

Bibliography

- [1] D. P. ATHERTON, *Almost six decades in control engineering*, IEEE Control Systems Magazine, 34 (2014), pp. 103–110.
- [2] A. M. BLOCH, *An introduction to aspects of geometric control theory*, in Nonholonomic Mechanics and Control, P. Krishnaprasad and R. Murray, eds., vol. 24 of Interdisciplinary Applied Mathematics, Springer, New York, NY, 2015.
- [3] F. BULLO AND A. D. LEWIS, *Geometric Control of Mechanical Systems*, vol. 49 of Texts in Applied Mathematics, Springer Verlag, New York-Heidelberg-Berlin, 2004.
- [4] I. CORNFELD, S. FOMIN, AND Y. SINAI, *Smooth dynamical systems on smooth manifolds*, in Ergodic Theory. Grundlehren der mathematischen Wissenschaften (A Series of Comprehensive Studies in Mathematics), vol. 245, Springer, New York, NY, 1982.
- [5] M. EIE AND S.-T. MINKING, *A Course on Abstract Algebra*, World Scientific, 2010.
- [6] S. FIORI, *Nonlinear damped oscillators on Riemannian manifolds: Fundamentals*, Journal of Systems Science and Complexity, 29 (2016), pp. 22–40.
- [7] ———, *Nonlinear damped oscillators on riemannian manifolds: Numerical simulation*, Communications in Nonlinear Science and Numerical Simulation, 47 (2017), pp. 207 – 222.
- [8] ———, *Non-delayed synchronization of non-autonomous dynamical systems on Riemannian manifolds and its applications*, Nonlinear Dynamics, 94 (2018), pp. 3077–3100.
- [9] R. FUENTES, G. P. HICKS, AND J. M. OSBORNE, *The spring paradigm in tracking control of simple mechanical systems*, Automatica, 47 (2011), pp. 993–1000.

- [10] S. GAJBHIYE AND R. BANAVAR, *The Euler-Poincaré equations for a spherical robot actuated by a pendulum*, IFAC Proceedings Volumes, 45 (2012), pp. 72–77. 4th IFAC Workshop on Lagrangian and Hamiltonian Methods for Non Linear Control.
- [11] V. GHAFARI AND F. SHABANINIA, *Synchronization of nonlinear dynamical systems using extended Kalman filter and its application in some well-known chaotic systems*, Nonlinear Studies, 25 (2018).
- [12] O. GOLEVYCH, O. PYVOVAR, AND P. DUMENKO, *Synchronization of nonlinear dynamic systems under the conditions of noise action in the channel*, Latvian Journal of Physics and Technical Sciences, 55 (2018), pp. 70–76.
- [13] I. KOVACIC AND M. BRENNAN, *The Duffing Equation: Nonlinear Oscillators and their Behaviour*, Wiley, 2011.
- [14] M. A. MAGDY AND T. S. NG, *Regulation and control effort in self-tuning controllers*, IEE Proceedings D – Control Theory and Applications, 133 (1986), pp. 289–292.
- [15] M. MOLAEI, *Hyperbolic dynamics of discrete dynamical systems on pseudo-Riemannian manifolds*, Electronic Research Announcements, 25 (2018), pp. 8–15.
- [16] F. MOLERO, M. LARA, S. FERRER, AND F. CÉSPEDES, *2-D Duffing oscillator: Elliptic functions from a dynamical systems point of view*, Qualitative Theory of Dynamical Systems, 12 (2013), pp. 115–139.
- [17] A. NÁVRAT AND P. VAŠÍK, *On geometric control models of a robotic snake*, Note di Matematica, 37 (2017), pp. 120–129.
- [18] M. NIELSEN AND I. CHUANG, *Quantum Computation and Quantum Information*, Cambridge University Press, 2004.
- [19] K. OJO, S. OGUNJO, AND A. OLAGUNDOYE, *Projective synchronization via active control of identical chaotic oscillators with parametric and external excitation*, International Journal of Nonlinear Science, 24 (2017), pp. 76–83.
- [20] J. M. OSBORNE AND G. P. HICKS, *The geodesic spring on the Euclidean sphere with parallel-transport-based damping*, Notices of the AMS, 60 (2013), pp. 544–556.
- [21] A. PRYKARPATSKY AND I. MYKYTIUK, *Algebraic Integrability of Nonlinear Dynamical Systems on Manifolds: Classical and Quantum Aspects*, Springer, 1998.

-
- [22] L. RIGHETTI, *Control and Synchronization with Nonlinear Dynamical Systems for an application to Humanoid Robotics*, Ecole Polytechnique Fédérale de Lausanne, 3 2004.
- [23] R. W. H. SARGENT, *Optimal control*, Computational and Applied Mathematics, 124 (2000), pp. 361–371.
- [24] N. SHERIF AND E. MORSY, *Computing real logarithm of a real matrix*, International Journal of Algebra, 2 (2008), pp. 131–142.
- [25] M. SHIINO AND K. OKUMURA, *Control of attractors in nonlinear dynamical systems using external noise: Effects of noise on synchronization phenomena*, Discrete and Continuous Dynamical Systems - Series S, (2013), pp. 685–694.
- [26] K. SREENATH, T. LEE, AND V. KUMAR, *Geometric control and differential flatness of a quadrotor UAV with a cable-suspended load*, in 52nd IEEE Conference on Decision and Control, Dec. 2013, pp. 2269–2274.
- [27] H. SUSSMANN, *Dynamical systems on manifolds: Accessibility and controllability*, in 1971 IEEE Conference on Decision and Control, Dec 1971, pp. 188–191.
- [28] V. VALIMAKI, J. NAM, J. SMITH, AND J. ABEL, *Alias-suppressed oscillators based on differentiated polynomial waveforms*, IEEE Transactions on Audio, Speech, and Language Processing, 18 (2010), pp. 786–798.
- [29] B. VAN DER POL, *The nonlinear theory of electric oscillations*, Proceedings of the Institute of Radio Engineers, 22 (1934), pp. 1051–1086.
- [30] S. VENTURINI, *Continuous dynamical systems on Taut complex manifolds*, Annali della Scuola Normale Superiore di Pisa - Classe di Scienze, Ser. 4, 24 (1997), pp. 291–298.
- [31] C. W. WU, *Synchronization in Complex Networks of Nonlinear Dynamical Systems*, World Scientific Publishing Co Pte Ltd, Singapore, October 2007.
- [32] M. ZAREI, A. KALHOR, AND M. MASOULEH, *An experimental oscillation damping impedance control for the Novint Falcon haptic device based on the phase trajectory length function concept*, Proceedings of the Institution of Mechanical Engineers, Part C: Journal of Mechanical Engineering Science, 233 (2019), pp. 2663–2672.
- [33] Z. ZHANG AND G. CHEN, *Liquid mixing enhancement by chaotic perturbations in stirred tanks*, Chaos, Solitons & Fractals, 36 (2008), pp. 144–149.

A. Heun-like and Runge-like algorithms

These methods have been implemented by us, trying to apply Heun and Runge-Kutta algorithms, based on first-order equations, to second-order equations. They were applied to the soft Duffing oscillator and they had been realized before the implementations of Heun and Runge because the existence of such methods for orders higher than the first was not known. The true methods apply to each of the two equations of the first order of the system the classical algorithm (a system of two equations of the first order is equivalent to a second-order equation), while in the one developed by us this division is not made, but in each point we are going to evaluate together position and vector field, trying to use the same principle used for first order systems. Moreover, the validity and correctness of these methods have never been verified, but since the results obtained seem reliable and comparable to those obtained with the methods of Heun and Runge-Kutta it was decided to preserve and show such simulations.

A.1 Heun-like algorithm

The time-discretized version of the dynamical system (4.11), implemented through the Heun-like method and associated to the soft Duffing potential reads:

$$\begin{cases} a_{1,k} := v_k, \\ \tilde{x}_{k+1} = \exp_{x_k}(a_{1,k} h), \\ a_{2,k} := \mathbf{P}^{x_k \rightarrow \tilde{x}_{k+1}} \left[v_k - h\mu(v_k^\top v_k)^{\varepsilon-1} v_k - h(-1 + \kappa d^2(x_k, r)) \log_{x_k}(r) \right], \\ x_{k+1} = \exp_{x_k} \left(\frac{a_{1,k} + \mathbf{P}^{\tilde{x}_{k+1} \rightarrow x_k}(a_{2,k})}{2} h \right), \\ v_{k+1} = \mathbf{P}^{x_k \rightarrow x_{k+1}} \left[v_k - h\mu(v_k^\top v_k)^{\varepsilon-1} v_k - h(-1 + \kappa d^2(x_k, r)) \log_{x_k}(r) \right], \end{cases} \quad (\text{A.1})$$

with $h > 0$ being a discretization stepsize for the dynamical system and $k = 0, 1, 2, \dots, \varepsilon$ being the exponential for nonlinear damping and $d^2(x_k, r)$ being the distance between any point x_k over the trajectory and the reference point r . Moreover, the system state is represented by the variable-pair $(x_k, v_k) \in T\mathbb{S}^{n-1}$ for any $k \in \mathbb{N}$.

The Figure A.1 illustrates the behavior of a soft Duffing oscillator, implemented through the Heun-like method, on the ordinary sphere \mathbb{S}^2 in the absence of a damping term. As expected, the state of this non-linear dynamical system oscillates around the reference point r . Moreover, the motion of the system continues endlessly due to the periodical conservation of the total energy.

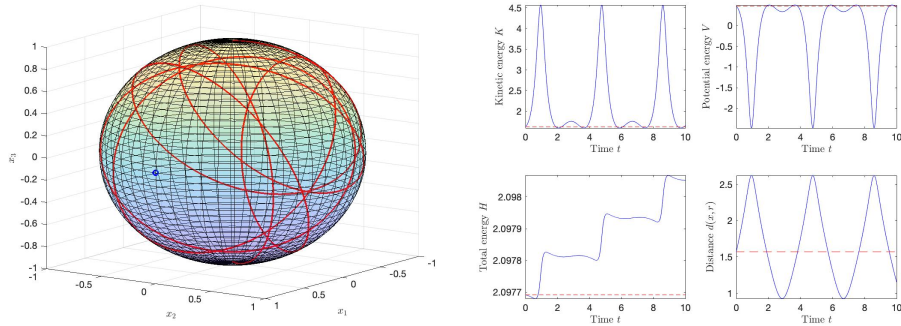


Figure A.1: *Behaviour of the soft Duffing (A.1) in the absence of non-linear damping (namely, $\mu = 0$), implemented through the Heun-like method. The left-hand side panel shows the trajectory in the space \mathbb{S}^2 , when the starting point is $x_0 = [0 \ 0 \ 1]^\top$, the reference point for the oscillator is $r = [1 \ 0 \ 0]^\top$ (denoted by a blue open circle) and the initial speed is $v_0 = [-1 \ -1.5 \ 0]^\top$. The parameters used in the simulation are $\kappa = 0.5$, $h = 0.0001$.*

A.2 Runge-like algorithm

The time-discretized version of the dynamical system (4.11), implemented through the Runge method and associated to the soft Duffing potential reads:

$$\begin{cases} a_{1,k} := v_k, \\ \tilde{x}_{k+1} = \exp_{x_k}(k_1 h), \\ a_{2,k} := \mathbf{P}^{x_k \rightarrow \tilde{x}_{k+1}} \left[v_k - h\mu(v_k^\top v_k)^{\varepsilon-1} v_k - h(-1 + \kappa d^2(x_k, r)) \log_{x_k}(r) \right], \\ x_{k+1} = \exp_{x_k} \left(h \mathbf{P}^{\tilde{x}_{k+1} \rightarrow x_k}(a_{2,k}) \right), \\ v_{k+1} = \mathbf{P}^{x_k \rightarrow x_{k+1}} \left[v_k - h\mu(v_k^\top v_k)^{\varepsilon-1} v_k - h(-1 + \kappa d^2(x_k, r)) \log_{x_k}(r) \right]. \end{cases} \quad (\text{A.2})$$

The Figure A.2 illustrates the behavior of a soft Duffing oscillator, implemented through the Runge-Kutta-like method, on the ordinary sphere \mathbb{S}^2 in the absence of a damping term. As expected, the state of this non-linear dynamical system oscillates around the reference point r . Moreover, the motion of the system continues endlessly due to the periodical conservation of the total energy.

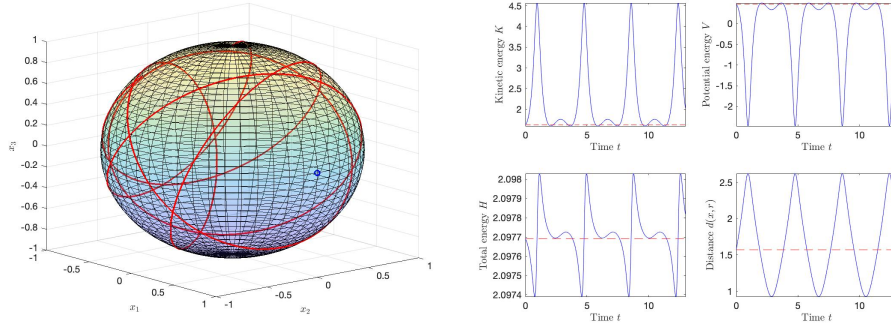


Figure A.2: Behaviour of the soft Duffing (A.2) in the absence of non-linear damping (namely, $\mu = 0$), implemented through the Runge-Kutta-like method. The left-hand side panel shows the trajectory in the space \mathbb{S}^2 , when the starting point is $x_0 = [0 \ 0 \ 1]^\top$, the reference point for the oscillator is $r = [1 \ 0 \ 0]^\top$ (denoted by a blue open circle) and the initial speed is $v_0 = [-1 \ -1.5 \ 0]^\top$. The parameters used in the simulation are $\kappa = 0.5$, $h = 0.0001$.

It can be seen that using these methods the total energy, which should be constant, oscillates slightly, with an error in the fourth decimal digit. Even if these methods are not “verified”, they present a smaller error than in Euler, and the results obtained seem reliable.

Acknowledgments

The present research work was completed while the author MI were taking an internship at the Agency for Science, Technology and Research (A*STAR, Republic of Singapore) during April-June 2019. The author wishes to gratefully thank Dr. Hwee Kuan Lee who made this internship possible.